Spring 2023

Multi-Uncrewed Underwater Vehicle (UUV) Optical Communication System Design

Igor Vladimirov
University of New Hampshire, Durham

Multi-Uncrewed Underwater Vehicle (UUV) Optical Communication System Design

BY

IGOR VLADIMIROV

BS Computer Engineering, U.S. Naval Academy, 2014

THESIS

Submitted to the University of New Hampshire

in Partial Fulfillment of

the Requirements for the Degree of

Master of Science

in

Ocean Engineering

May, 2023

This thesis/dissertation has been examined and approved in partial fulfillment of the requirements for the degree of Master of Science in Ocean Engineering by:

Thesis Director, Dr. May-Win Thein, Professor (Ocean and Mechanical Engineering)

Dr. Yuri Rzhanov, Research Professor (Ocean Engineering and Center for Coastal and Ocean Mapping)

Dr. Martin Renken, Research Scientist (Signal Processing)

On 14 December 2022

Original approval signatures are on file with the University of New Hampshire Graduate School.

ACKNOWLEDGEMENTS

This project brought many challenges and many learning opportunities, and its successful completion is due to help and contributions of faculty, staff and peers. I want to express gratitude to the following people:

- Professor May-Win Thein - thank you very much for accepting the challenge of being my advisor. You provided me with everything I needed to be successful while at UNH: equipment, lab space, resources and much more. This project's success is due to your leadership and guidance.
- Dr. Yuri Rzhanov - thank you for guiding me through a challenging field of optics and light attenuation, a topic I never worked with prior to this research. Your expertise was vital to my success.
- Dr. Martin Renken - thank you for instilling accountability in my work as well as work of my peers. Your direct and constructive feedback pushed us beyond our capabilities and produced excellent results.
- Eric Seeley - your creative ideas turned this design from a dumpster fire into an efficient and reliable system (on many occasions). Your knowledge and willingness to help are a significant contribution to my success. Thank you!
- Nick Custer - thank you for taking me under your wing and being my big brother throughout my time at UNH. Your mentorship (both academic and professional) pushed me through the program (and especially the tough times).

- Ozzy Oruc - thank you for your support on the mechanical engineering side! Without you, the waterproof integrity of this system would be nowhere.

- Derrek Perham - thank you for your support during the experiments! You were there for every single one of them. It takes a lot to efficiently deploy a system on repetitive basis, and because of you and your support we never had a "bad" deployment.

- Hannah Arnholt - thank you for providing a quick and effective jump start into my research. You led me to a successful thesis problem/topic, which paved the path for my research timeline and successful project completion despite the short timeline.

- Josh Girgis - thank you for your help and guidance during the most challenging time of research (the beginning). Because of you, I was able to setup our first "lab" in the middle of a graduate study hall.

The list of people goes on, and many are not mentioned above. I will be forever grateful for your care, support, love and mentorship. Thank you!

TABLE OF CONTENTS

ABSTRACT

MULTI-UNCREWED UNDERWATER VEHICLE (UUV) OPTICAL COMMUNICATION SYSTEM DESIGN

by

Igor Vladimirov

University of New Hampshire, December, 2022

Over the past few decades the state of art of Uncrewed Underwater Vehicles (UUVs) has grown significantly, and one of the major challenges remains establishing reliable underwater communication among UUVs. This case is especially true in a multi-UUV setting where tethered communication is not an option. This research focuses on designing a cost-efficient, short distance optical communication system capable of supporting formation control of multiple UUVs. Although light attenuation underwater significantly degrades communication ranges, experimental results show that optical communication can achieve distances of almost 20 meters in clear water by utilizing a simple 10-Watt LED transmitter (with larger distances being tenable given more powerful light sources). Furthermore, a signal processing scheme and protocol is designed and tested. This scheme includes a timing sequence capable of supporting multiple UUVs, all utilizing the same transmitter wavelength and carrier frequency. This optical communication scheme is tested in air in a static three-node network. All nodes are able to send, receive and interpret digital packets at a speed of 5kbps. Although further fine-tuning of the system is required due to divergence angle limitations and timing

inefficiencies, the experiments presented in this work show a successful proof-of-concept of a short distance multi-UUV optical communication system

CHAPTER 1

Introduction

1.1 Overview of Uncrewed Underwater Vehicles (UUVs)

In today's world human technology is growing at incredible rates, enabling our society to explore and study the underwater world which was unfathomable 100 years ago. Today we can access depths of over 6,000 meters and utilize ocean and maritime environments for a variety of tasks: power distribution from offshore wind farms, gas/oil extraction, research, farming, military and defense applications and much more [1]. Most of these capabilities exist due to state-of-the-art Remote Operating Vehicle (ROV) technology. Human divers do not operate below depths of 1000 feet. And, even at or above 1000 feet, the risks of death or permanent disabilities are significant [2]. Therefore, robots are utilized as they are able to access much greater depths without risking our health and well being.

One of the major challenges of working with autonomous underwater vehicles is establishing a reliable communication between those vehicles as well as between each vehicle and ground/shore stations from which they are deployed. This issue arises because water is a much denser medium than air. It possesses high electrical conductivity, which influences water's damping properties, and causes the absorption of electromagnetic waves used for wireless communication in air [3]. Therefore engineers and scientists are constantly seeking creative ways to transmit data underwater.

1.2 Current Communication Methods Utilized by Underwater Vehicles

As mentioned above, it is challenging to establish a reliable communication network underwater, where typical radio and GPS applications utilized on the surface will not propagate. A good example of this statement was demonstrated by a group of scientists from Ilmenau, Germany, who utilized two 2.4GHz antennas to measure communication signal strength underwater. Here, most of the signal was lost at ranges greater than 10cm [3]. Most common communication methods utilized for control of underwater vehicles today include attached tethers, acoustic and optic modems [4]. In cases where a vehicle is remotely controlled by a human (ROV), tethered communication is most common [4]. A tether is connected from the shore station or a ship to the remote vehicle and is utilized to control the vehicle, as well as send and receive various data signals to accommodate the mission. Even though in most cases this approach meets all mission requirements, tetherless ROVs are currently being developed [5], as the tethered approach is not feasible when deploying a swarm of multiple UUVs due to path obstructions and cable entanglements [4]. Wiring multiple robots to one another severely restricts maneuverability. Therefore, other methods are utilized to resolve this problem.

The most common way to establish wireless communication in underwater environment is done via acoustics [4]. Depending on frequency and amplitude, sound waves can travel underwater for miles. The concept of acoustic communication is based on creating certain patterns of vibrations at the transmitter (piezoelectric transducer), which then create pressure waves that propagate through the water medium [6]. Today's acoustic modems can employ low-frequency pulses (9-13kHz) to achieve communication ranges of greater than 5km [7]. Teledyne Benthos and OceanServer Technology have demonstrated reliable communication at ranges greater than 1.7km between submerged compact underwater vehicle and a shore station. The system was operated at a frequency ranges of 22-27kHz and communication rate of 600bps [7]. Acoustic communication, although widely used, is limited to

the speed of sound (roughly 1500 m/s and varies with factors such as pressure, temperature and salinity), which limits transmission speed [6]. Even though acoustic underwater communication method is the only reliable method to communicate over 200m distances today, it is limited by geometric spreading, absorption, propagation delays, and noise (turbulence, wind-driven waves, shipping traffic, thermal noise) [8]. Additionally, acoustic systems suffer from multi-path arrivals due to surface and bottom interactions in shallow waters [9].

Even though the last decade has seen many studies and improvements in various underwater network and protocol schemes, most transmission speeds are still low. Today's modems typically do not exceed 10kbps, with most operating in ranges of 1000bps or under [10]. Because of these challenges acoustic modems and transducers must be tuned precisely, which makes them complex and more costly, even for low-speed packages [10].

Electromagnetic waves present another way to establish underwater wireless communication. Visible light travels much faster than sound ($c_{light} = 3 \times 10^8$ m/s) and therefore presents an opportunity for communication speeds, which are orders of magnitude faster than that of acoustics [4]. As such, visible light communication (visible light spectrum of 400-700nm) has been a topic of interest over the past two decades. Visible light attenuates non linearly in water, and its absorption depends on the light's wavelength [11]. Figures 1.1 and 1.2 show an overview of attenuation of visible light in pure seawater. In addition to the wavelength, water conditions, such as turbidity and turbulence, greatly affect light propagation [12].

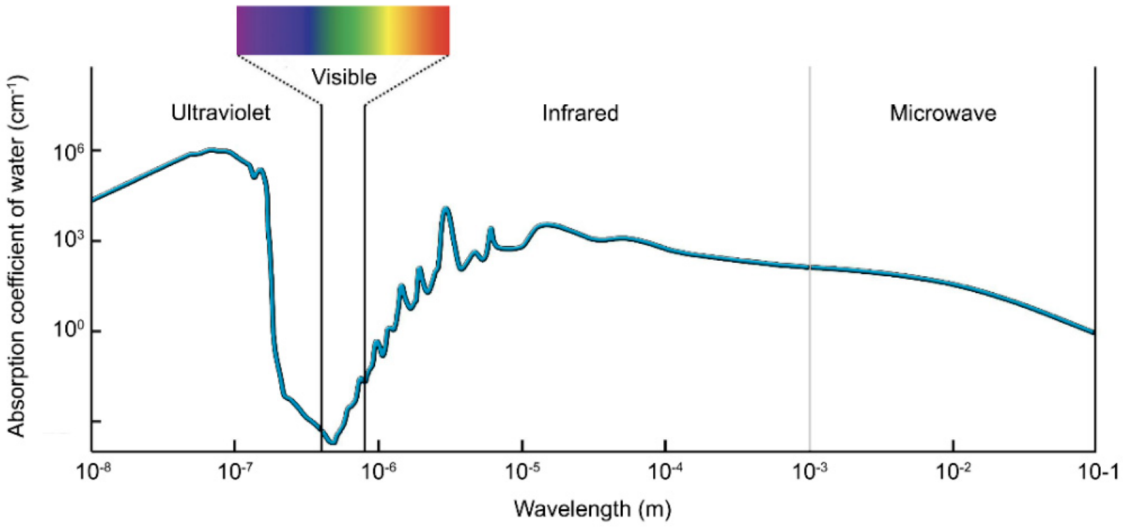

Figure 1.1: Absorption coefficient of pure seawater for different transmission wavelengths [12]

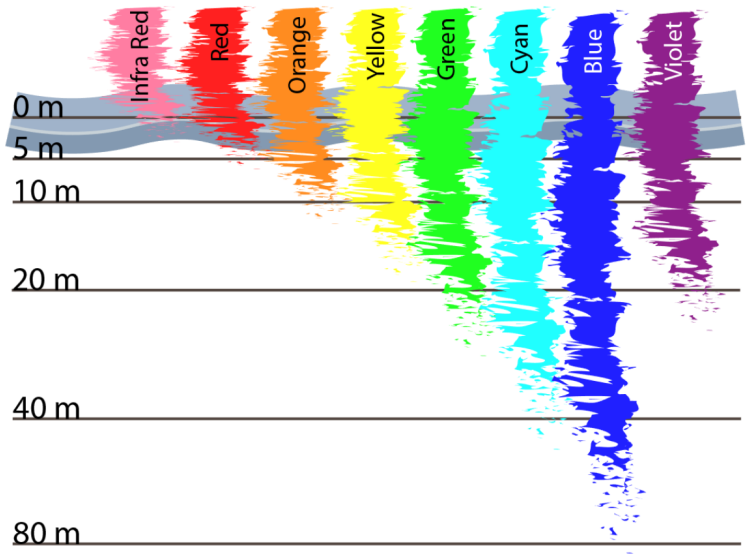

Figure 1.2: Typical propagation of visible light in clear water [13]

Various schemes exist that utilize laser diodes and LEDs as light sources. Lasers offer high-modulation bandwidth (communication speeds are in GHz range) but have a narrow divergence which requires precise pointing between transmitter and receiver. Over the past decade, communication rates of 2.7Gbps was demonstrated at a range of 34.5m via a laser

transmitter in clear water utilizing On-Off-Keying (OOK) [14], and ranges of 120m were achieved via a pulse laser with peak power of $10^5 W$ [14]. LEDs, on the contrary, offer high-power efficiency, cost efficiency and longevity but suffer higher attenuation due to wide light divergence. In the past, a 50m range was achieved at a data rate of 2.28Mbps in clear water via a transmitter comprised of eighteen LEDs [14]. Because underwater optic communication systems are significantly limited by range, various studies today explore options of hybrid optic-acoustic communication systems [12].

As briefly shown in Figure 1.1, light attenuation in seawater is at its minimum for the blue/green light spectra ($\lambda = 460nm$) in clear water, and the most effective propagated wavelength increases towards the green range ($\lambda = 540nm$) for coastal waters. This phenomenon occurs, in part, because phytoplankton chlorophyll pigments absorb light in the blue and red spectral wavelengths.

In general, the spectral beam attenuation coefficient $c(\lambda)$ can be described as $c(\lambda) = a(\lambda) + b(\lambda)$, where $a(\lambda)$ represents the absorption coefficient, and $b(\lambda)$ represents the scattering coefficient. Both absorption and scattering are a function of wavelength λ and determined by the concentration of water molecules, particulate algal and sediment matters, and colored organic solvents [12]. Table 1 provides typical values of these coefficients for various water types.

Water Types	C **(mg/m^3)**	$a(\lambda)$ **(m^{-1})**	$b(\lambda)$ **(m^{-1})**	$c(\lambda)$ **(m^{-1})**
Pure sea water	0.005	0.053	0.003	0.056
Clear ocean water	0.31	0.069	0.08	0.151
Costal ocean water	0.83	0.088	0.216	0.305
Turbid harbor water	5.9	0.295	1.875	2.170

Table 1: Typical attenuation, absorption and scattering values in different water types for $\lambda = 532nm$ [12]

Because of large attenuation values presented above, there are no existing systems capable of obtaining long distance optical underwater communication. There are, however, various models in development for short and medium ranges. For example, Hydromea offers a variety

of optical modems capable of ranges up to 30m with data rates up to 10Mbps [15].

Optical configurations can be classified into two groups: Diffused Line Of Sight (LOS) and point-to-point LOS. The diffused LOS configuration presents wide source spreading, which offers wide divergence angle (tens of degrees for LEDs compared to 2mrad or less for lasers [16]) but suffers high attenuation, which leads to a low transmission data rate (Gbps range for laser vs. Mbps range for LEDs [14]). Point-to-point LOS, on the contrary, offers high data rates but requires precision pointing, which is a major issue for non-stationary nodes. Both examples are illustrated in Figure 1.4.

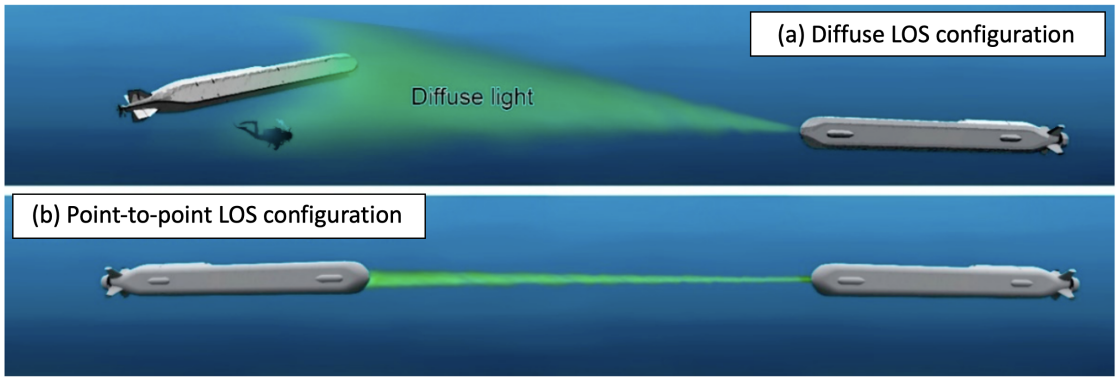

Figure 1.4: Examples of optical communication configurations [12]

The techniques utilized to capture and read visible light signals involve various types of photo detectors. Typically PIN and Avalanche photodiodes are utilized, and both will be discussed in detail in Chapter 3 [17]. In addition to strong light attenuation under water, high photodiode detection thresholds and high noise intensity linked to transimpedance amplifier results in photodiodes being a poor option for long-distance underwater communication [12]. Typical underwater optical communication configurations are limited to a range of 100 meters. Although there is an ongoing research on developing receivers that utilize Single Photon Avalanche Diodes (SPADs), which may significantly improve optical communication ranges, these sensors are in their early stages of development and require further studies [12].

1.3 Performance Issues With Wireless UUV Communication Today

Although research in underwater wireless optic communication has been ongoing for the past two decades, it remains a relatively new concept with performance issues due to the aforementioned reasons. One of the shortfalls in today's state of art is the lack of reliable communication methods between multiple, collaborative autonomous UUVs. There are many examples of optical communication papers which include light propagation and basic transmitter and receiver designs. For example, Heather Brundage developed an optical system capable of transmitting data at 3Mbps via a laser transmitter over a distance of 13m [17]. This design demonstrates great capabilities of point-to-point LOS, stationary optical configuration but does not take into account dynamic node configuration. Additionally, this design did not include any data processing or communication protocols utilized, which are vital for a multi-node network. To the author's knowledge, there is currently no existing adapted optical communications protocol that exists for multi-UUV collaborative missions.

As optical research is progressing there are various industries offering wireless underwater products. For example, Hydromea offers a variety of optical underwater modems capable of data transmission of 10Mbps for up to 30 meters [15] and, as of 2022, a world's first optically-controlled, wireless ROV designed for flooded confined spaces [5]. Figure 1.5 shows Hydromea's LUMA X-UV modem and EXRAY optical ROV.

Figure 1.5: Hydromea LUMA X-UV optical modem (left) [15] and EXRAY tetherless drone (right) [5]

Although this technology offers great potential in multi-UUV communication, all infor-

mation is proprietary.

This research focuses on the design and modeling of a cost-effective wireless optical communication system and protocol for multi-UUV missions:

- This work considers light propagation in the development of the transmitter and receiver design, circuit analysis, and digital signal processing.
- An optical communications system is designed for basic multi-UUV networking for non-turbulent waters. The design consists of a short-range, diffuse LOS LED transmitter configuration and a PIN photodiode receiver configuration.
- This work proposes a complete communication system design and protocol, which can be implemented to control UUVs in various short range applications.
- An experimental proof-of-concept of all subsystems is provided, which shows the proposed optical communication system as viable for future full integration.

1.4 Thesis Outline

Chapter 2 reviews basic light attenuation, transmitter source selection and transmitter source design. Chapter 3 provides an introduction to photodiodes, proposed solution to ambient light noise and receiver circuit design. Chapter 4 presents experimental results for light propagation of multiple light wavelengths (colors). Chapter 5 describes the digital processing of incoming message traffic, to include timing, packet structure and bit-error-rate experimental results. Digital signal processing and time-division multiplexing scheme applied to a network of multiple UUVs is discussed in Chapter 6, which also presents the experimental results of the applied underwater optical communications system for a static, three-node network.

CHAPTER 2

Underwater Transmitter Design

2.1 Underwater Light Attenuation

This chapter covers attenuation of the visible spectrum of electromagnetic radiation (i.e., visible light). Visible light attenuation underwater is dependent upon two main factors: absorption and scattering. Absorption is a thermodynamic process that varies non linearly with the light's wavelength, while scattering is a mechanical process that changes direction of the photons [11]. Both of these coefficients vary with factors, such as dissolved substances and organic matter [11]. In summary, underwater light attenuates exponentially based on Beer-Lambert's Law for light power as a function of wavelength:

$$P(\lambda) = P_0(\lambda)e^{-\alpha(\lambda)l} \tag{2.1}$$

Where $P_0(\lambda)$ represents the initial light power at wavelength λ, $\alpha(\lambda)$ represents the light attenuation coefficient, and l is the distance from light source [11]. Additionally, light attenuation coefficient $\alpha(\lambda)$ can be calculated as follows:

$$\alpha(\lambda) = \alpha_a(\lambda) + \alpha_s(\lambda) \tag{2.2}$$

Where $\alpha_a(\lambda)$ is the water absorption coefficient, and $\alpha_s(\lambda)$ is the scattering coefficient [11]. Recent data analysis by IPB University scientists provide a good overview of light propagation in various water types [18]. Light attenuation was analyzed throughout various locations of Northeast Gulf of Mexico in order to describe variations of one optical depth

and attenuation coefficients for different water types and light wavelengths [18]. Northeast Gulf of Mexico is known for its dynamic water characteristics due to the input of fresh water from several rivers, Loop current, local winds and upwelling, all of which greatly affect variability of chlorophyll, dissolved colored organic matter, and other organic matter and particulates. As a result, this region serves as a good location to test and describe light attenuation variability with different water types [18]. Submersible Marine Environmental Radiometers (MER) were installed at various locations as depicted in Figure 2.1.

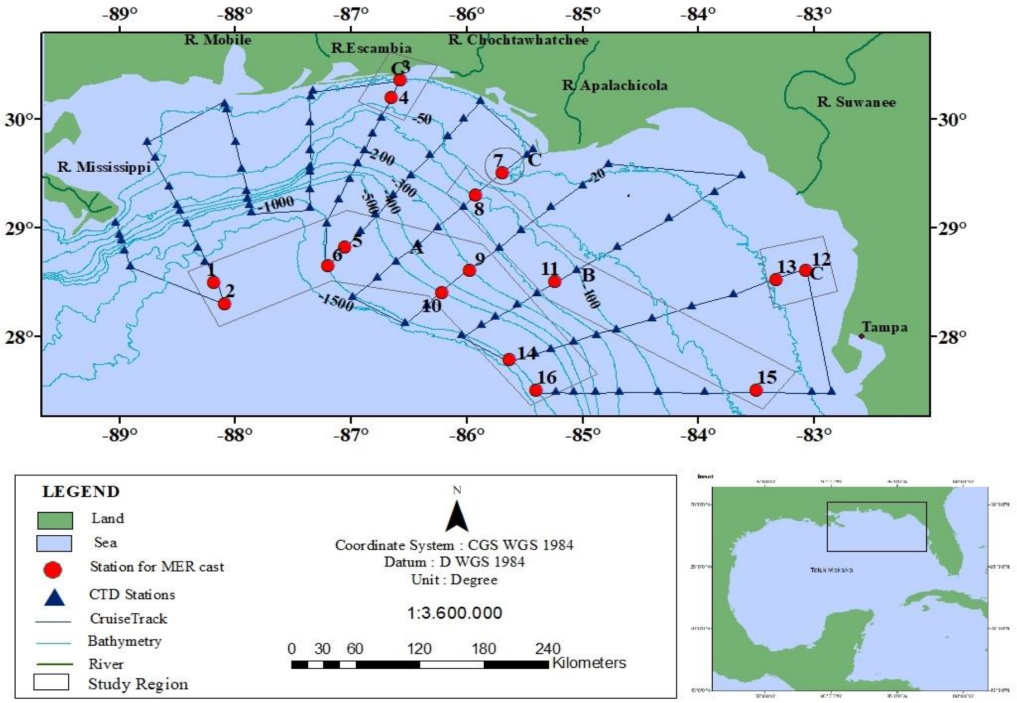

Figure 2.1: Map of research sites in the Northeast Gulf of Mexico [18]

Three different water types were analyzed [18]:

- Region A - Offshore waters, where optical variability is dominantly influenced by variability of phytoplankton concentrations
- Region C - Inshore waters, where inherent optical properties are influenced by variability of concentration of phytoplankton, suspended solids, inorganic particles and organic matter

- Region B - Intermediate waters that transition between regions A and C

The goal of this experiment was to gain a better understanding of one optical depth. An optical depth is defined as that where the total amount of light (per wavelength) is found to be 37 percent of the light intensity as that at the surface. The one depth unit is an important concept in ocean color remote sensing because it limits satellite detection. One depth shows how clear the water column is and how deep the ocean color satellite sensor can receive signals [18]. In order to determine one depth, MER sensors at each stations were utilized to determine diffuse down welling attenuation coefficients, which are analogous to light attenuation coefficients described in equation (2) [18]. MER sensors were placed at depths of 50-60m for offshore waters, 40-55m in intermediate waters, and 10-30 meters in inshore waters. The following wavelengths (in nanometers) were measured for downwelling irradiance and depth data: 380, 412,443, 455, 475, 490, 510, 532, 555, 589, 665, 683. Collected data of initial and detected light intensities was utilized to calculate optical one depth values for each wavelength tested. In general, calculated results showed red colors to be shallowest, increasing with the green spectrum, maximum at the blue, and decreasing again with violet [18]. Figure 2.2 shows the one depth summary for each water type.

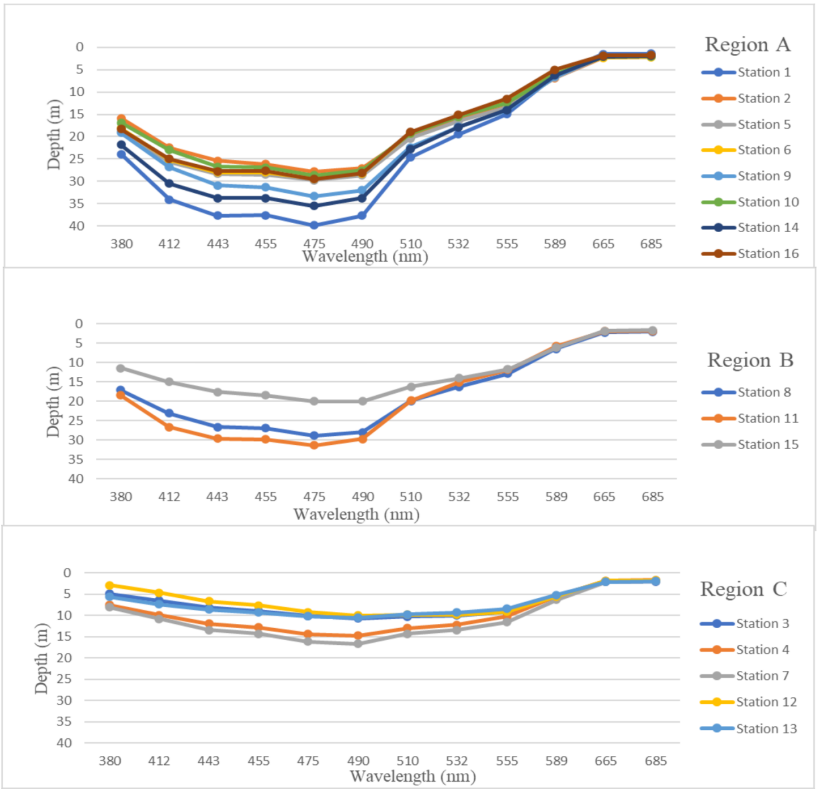

Figure 2.2: Calculated one optical depth values for various wavelengths throughout Northeast Gulf of Mexico [18]

In summary, the above results show the following [18]:

- Red wavelengths (589-683nm) attenuated in similar quantities in all waters at approximately 1.7-2.3m.
- Green wavelength (490-555nm) one depth was higher in offshore waters (11.5-24.6m), decreased in intermediate waters (11.7-19.9m), and was lowest in inshore waters (9.3-14.3m). Results varied with concentration of organic matter in waters.
- Blue wavelengths (443-475nm) showed the deepest values of 25.4-39.8m offshore, 17.6-31.3m in intermediate waters and 6.6-16.1m in inshore waters.
- Violet wavelengths (380-412nm) showed deepest values in offshore waters and decreased in intermediate and inshore waters.

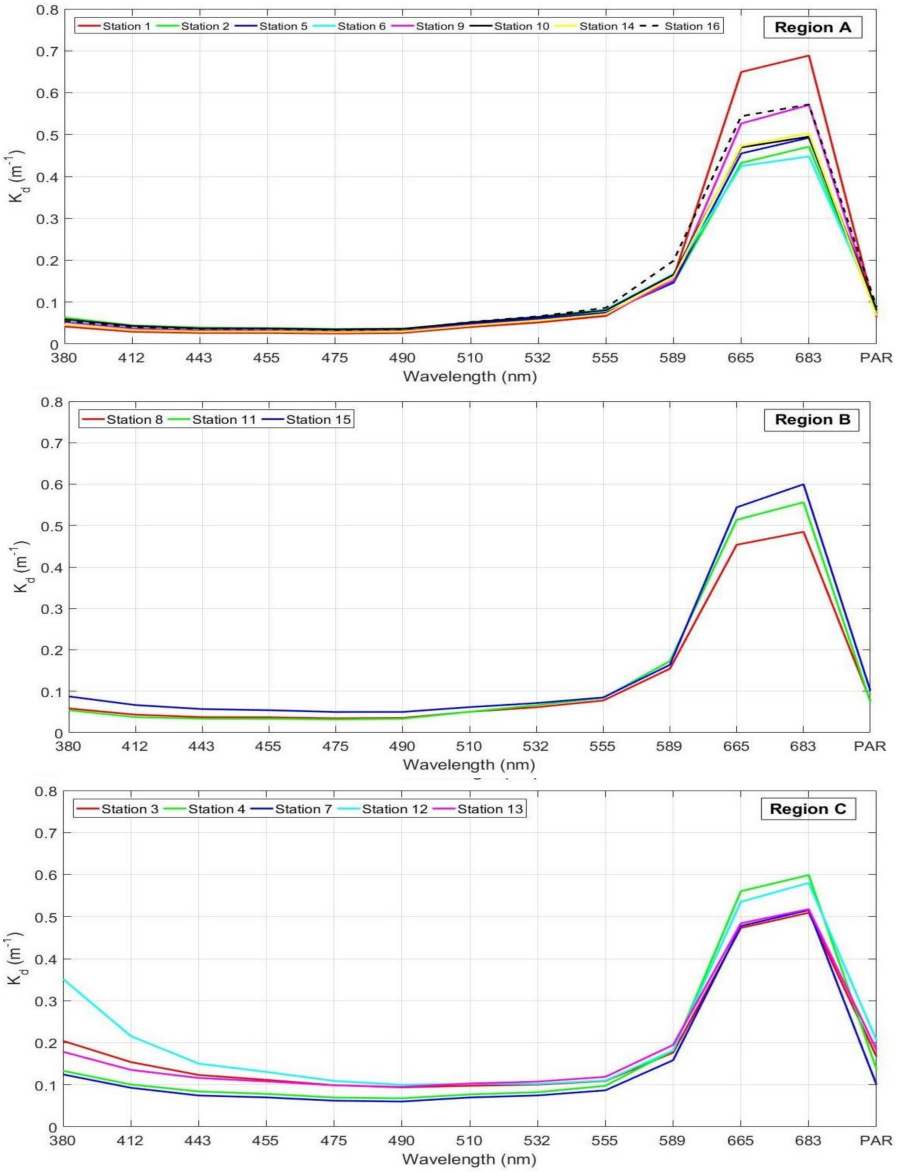

Figure 2.3: Attenuation coeficient (Kd) values derived from analyzed data [18]

As mentioned above, one depth values are analogous to that of light attenuation coefficient, which were also derived in this experiment and are shown on Figure 2.3. Overall, blue-green spectra shows the best results in all three types of water, and violet came close to blue-green wavelengths in offshore and intermediate waters at 400-412nm wavelengths. Significant variation is present in inshore waters. Attenuation increases significantly for red spectra, which would therefore, be a poor choice for an optical underwater transmitter. The work in this study uses this data to select an appropriate light source and calculate its

predicted attenuation.

2.2 Selecting a Light Source and Calculating Predicted Performance

Establishing a Line Of Sight (LOS) between dynamic objects at various angles is critical for underwater multi-UUV communication. Therefore, a point-to-point LOS configuration and the use of laser diodes is not a good option for this project. A diffuse light configuration with an LED source, instead, is selected for UUV communication. Based on the data of Nababan et. al, wavelengths of green, blue and UV/violet are selected for further consideration. LEDs for those three colors with respectively (approximate) similar parameters are chosen. Specifically, 10W Chanzon LEDs are selected due to their cost effectiveness ($5 per unit) and wide range of available wavelengths. Chanzon LED specifications are shown on Figure 2.4 [19], and the LED is shown in Figure 2.5 (left).

Power	Color	Color Temperature Wavelength	Forward Voltage	Forward Current	Luminous Flux
10W (3x3)	Warm White	3000-3500K	9-11V	840-1000mA	900-1000LM
	Natural White	4000-4500K	9-11V	840-1000mA	900-1000LM
	White	6000-6500K	9-11V	840-1000mA	900-1000LM
	Cool White	10000-15000K	9-11V	840-1000mA	900-1000LM
	Red	620-625nm	6-7V	840-1000mA	350-450LM
	Blue	460-470nm	9-11V	840-1000mA	90-100LM
	Cyan	490nm	9-11V	840-1000mA	120-130 LM
	Green	520-525nm	8-10V	840-1000mA	600-800LM
	Yellow	590-592nm	6-7V	840-1000mA	450-500LM
	Orange	600-605nm	9-11V	840-1000mA	600-700LM
	UV/Purple	395-400nm	9-12V	800-900mA	/
	Royal Blue (Grow LED)	440-445nm	9-11V	840-1000mA	90-100LM
	Deep RED (Grow LED)	660nm	6-7V	840-1000mA	350-450LM
	Full Spectrum (Grow LED)	380-840nm	9-11V	840-1000mA	200-300LM
	IR(730nm)	730-740nm	6-7V	840-1000mA	/
	IR(850nm)	850nm	5-6V	840-1000mA	/
	IR(940nm)	940nm	4.5-5.5V	840-1000mA	/
	RGB	R: 620-630nm G: 520-525nm B: 460-465nm	R:6-7V G:9-11V B:9-11V	R:280-350mA G:280-350mA B:280-350mA	R:90-100LM G:120-130LM B:30-40LM

Figure 2.4: LED specifications from Chanzon (selected LEDs in red) [19]

The three colors selected are: UV/purple ($395nm < \lambda < 400nm$), blue ($460nm < \lambda < 470nm$) and green ($520nm < \lambda < 525nm$). In order to resolve wide-source spreading and to enable a wide divergence angle, a condenser lens is selected and sized to match the LED

and transmitter's watertight tube. The Edmund Optics 50mm lens is shown in Figure 2.5 (right).

Figure 2.5: Chanzon 10W LED (left) [19] and Edmund Optics 50mm condenser lens (right) [20]

Condenser lenses are designed for illumination applications and are commonly used in emitter-detector applications [20]. In this case, the purpose of the condenser lens is to further spread the light beam and allow a wider divergence angle for both transmitter and receiver. Combined LED-lens product is shown in Figure 2.6.

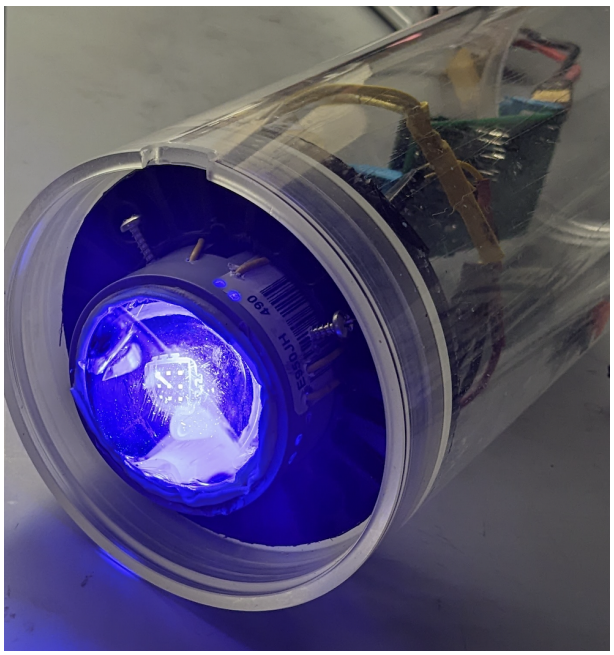

Figure 2.6: Optic transmitter

In order to model projected light attenuation underwater the Beer-Lambert law of Eq.(1) is used:

$$P(\lambda) = P_0(\lambda)e^{-k(\lambda)d} \tag{2.3}$$

$P_0(\lambda)$ is transmitter's initial intensity (10W), $k(\lambda)$ is the total underwater attenuation coefficient (wavelength dependent), and d is the distance between the transmitter and the receiver [11]. Eq.3 models power attenuation but does not include light dispersion caused by the divergence angle (Figure 2.7).

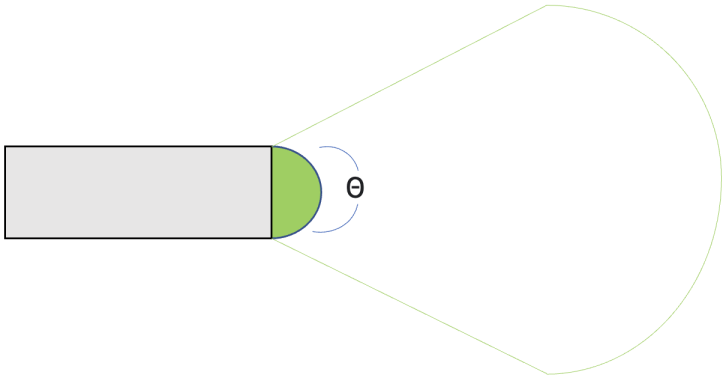

Figure 2.7: Transmitter light dispersion angle θ

Dispersion angle θ is calculated via an experiment, where transmitter's reflected light radius is measured as the source is moved a certain distance away from a solid medium. θ, calculated via basic trigonometry and collected measurements, is found to be 73.74°. Next, transmitter's light diameter (in inches) is calculated to be the following:

$$Diameter_{tx}(d) = Diameter_{tx0} + 2d \cdot tan\left(\frac{\theta}{2}\right) \tag{2.4}$$

Where $Diameter_{tx0}$ is the transmitter watertight tube's diameter of 3.63 inches (to be discussed in greater detail in the following sections), d is the distance between the transmitter's condenser lens and a receiver, and θ is the transmitter's dispersion angle of 73.74°. Due

to short communication ranges of less than 20 meters, a spherical attenuation of light is assumed with light intensity equal throughout the sphere with a surface area of:

$$A_{surface,sphere} = 2\pi \cdot \left(\frac{Diameter_{tx}(d)}{2}\right)^2 \tag{2.5}$$

Even though LED lights are much more efficient in comparison to other available light sources (e.g. incandescent and fluorescent bulbs), they are still less than ideal. Furthermore, a portion of its drawn electrical power is converted into heat and other forms of energy. For this thesis, LED efficiency approximation is selected to be 90 percent as per the Pennsylvania State University Center of Nanoscale Science MRSEC [21]. Another factor taken into consideration is the light's duty cycle. The transmitter pulses on and off at a 50% duty cycle (modulation details to be discussed in the next subsection), which dims the light source by 50%. Based on the above considerations and Eq.2.3-Eq.2.5, the following transmitter performance equation is derived:

$$I(\lambda, d) = \frac{P_0(\lambda) \cdot DutyCycle \cdot \eta_{LED} \cdot e^{-k(\lambda)d}}{A_{surface,sphere}} \tag{2.6}$$

$I(\lambda, d)$ is the projected light intensity W/m^2, $P_0(\lambda)$ is light's initial power of 10W spread over the transmitter's initial area of the watertight tube with $Diameter_{tx0} = 3.63in$, η_{LED} is LED efficiency of 90%, DutyCycle is 50% (fraction of time LED is on during its operation), and $A_{surface,sphere}$ is the surface area of light's spherical spreading discussed previously [11]. The main source of variable in Eq.2.6 is the total underwater attenuation coefficient $k(\lambda)$, which varies drastically in different water environments as discussed in Section 2.1 and has significant effects on optical communication system's performance. In order to test the validity of Equation 2.6, water in the University Of New Hampshire's (UNH's) Chase Engineering Tank is analyzed and $k(\lambda)$ is estimated.

The UNH Ocean Engineering Tank offers a 20ft-deep testing facility, which is utilized to validate projected system performance (details to be discussed in Chapter 4). Test tank

water is tested and compared to pure water (deionized water) to estimate the attenuation coefficient. To conduct this experiment, Ocean Optics equipment suite is utilized, including the USB-2000 spectrometer and a CUV-UV-10 sample holder (setup diagram shown in Figure 2.8).

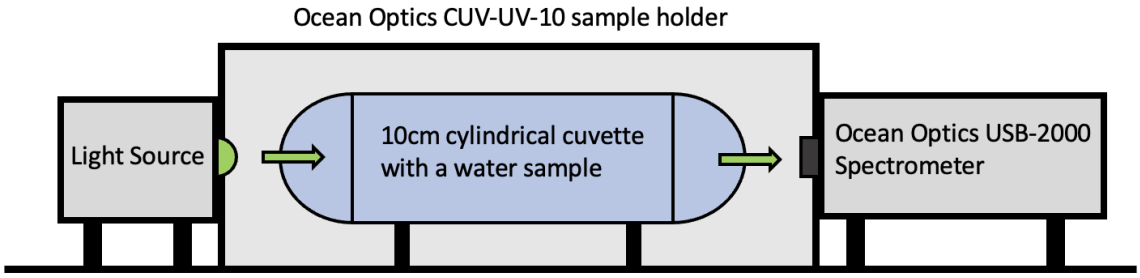

Figure 2.8: Experimental setup for attenuation coefficient

A light is placed in a fixed position, propagating through a cuvette filled with water and is captured on the other end of the cuvette via a spectrometer. Two samples of water are tested: deionized water (represents pure water) and UNH test tank water. Light and environmental conditions are kept constant for both samples, and multiple recording are taken.

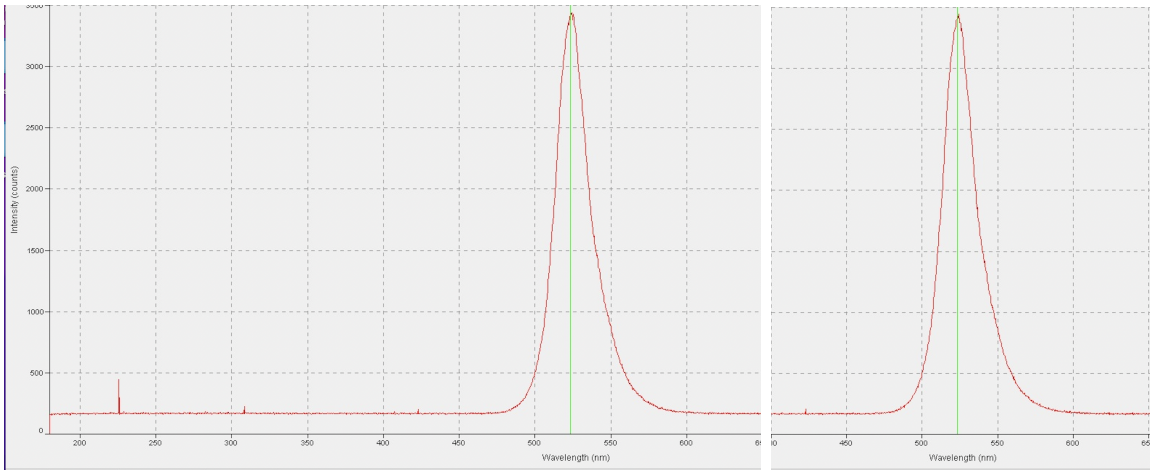

Figure 2.9: Spectrometer readings from cuvette experiment: deionized (left), UNH tank (right)

On average, the intensity for both water samples show similar results, and percent attenuation of tank water in comparison to deionized water is negligible. Deionized water shows an intensity range of 3285-3420 counts, while UNH tank water shows a range of 3350-3400 counts. Because both results closely resemble each other, a pure water absorption coefficient is assumed for the UNH test tank water.

Numbers from 1997 experiment by Optical Society of America are utilized to provide a reliable model of pure-water coefficients, where a spectral absorption of pure water (340-640nm) was measured with a Photothermal Deflection Spectroscopy (PDS) method [22]. The PDS method utilized a continuous-wave laser beam propagating through the fluid. Its deflection by refraction in the dynamic temperature-index gradient was proportional to that of the absorption coefficient [22]. PDS yielded the following numbers [22]:

- $\alpha_a(\lambda = 400nm) = 0.0087m^{-1}$ with 11% error
- $\alpha_a(\lambda = 470nm) = 0.0124m^{-1}$ with 11% error
- $\alpha_a(\lambda = 520nm) = 0.0488m^{-1}$ with 12% error

The PDS technique is insensitive to scattering and only yielded absorption coefficients [22]. Even though scattering in almost pure water is much smaller relative to absorption, it cannot be considered insignificant. From data presented in Section 2.1, scattering in pure seawater is less than 6% and grows significantly with turbidity and turbulence. Using conservative estimates, reflection coefficients of the UNH tank are assumed to be 10% of the total attenuation value, and all absorption coefficients include the aforementioned uncertainty errors. The following attenuation coefficients are utilized for the UNH engineering tank experiment:

- $k(\lambda = 400nm) = 0.0107m^{-1}$
- $k(\lambda = 470nm) = 0.0152m^{-1}$

- $k(\lambda = 520nm) = 0.0605m^{-1}$

Figure 2.10 shows projected light transmission of the transmitter utilized for this experiment (experimental setup and results are discussed in Chapter 4).

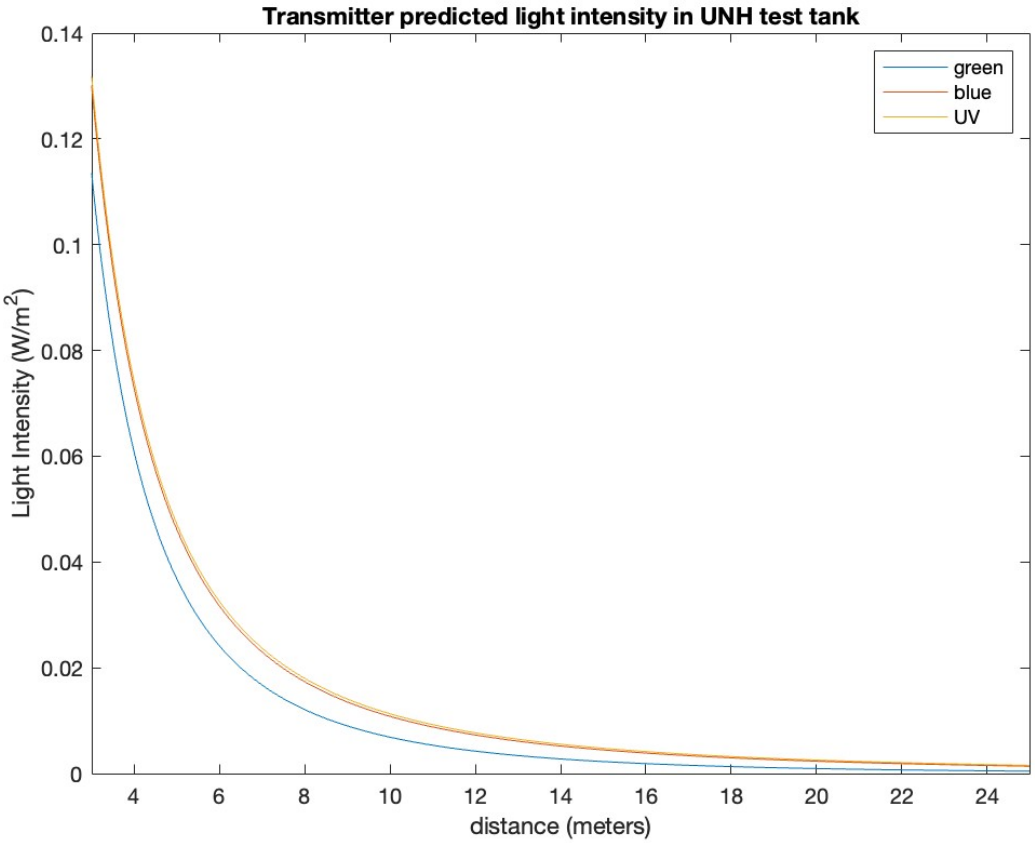

Figure 2.10: Predicted light attenuation values of the transmitter utilized in this experiment.

2.3 Transmitter Circuit Design

Most photodiode circuits are prone to ambient noise, which changes with the amounts of ambient light present in the environment [23]. Frequent changes in ambient light and resulting photodiode noise are expected during UUV movement. Therefore, a typical On-Off Keying (OOK) transmission would be challenging to interpret and is not a good option for this design. In order to address this issue, amplitude modulation is applied to modulate the signal to a more practical frequency range (100-300kHz). A carrier wave is chosen to

drive the LED, and the signal is filtered upon arrival at the receiver. A 555-timer circuit is designed to accomplish this task. A 555-timer is an oscillator with stability approaching 1%, even when varying supply voltages. In short, it is a small kit containing comparators, gates and flip-flops and is an ideal chip to produce an accurate square wave [24].

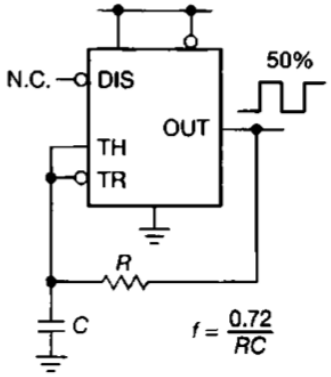

Figure 2.11: CMOS 555 oscillator 50% duty cycle square wave circuit [24]

An LM555CN CMOS 555 oscillator is utilized to design a 300kHz carrier square wave (Figure 2.11) with resistor, R, and capacitor, C, sizes to satisfy $f = \frac{0.72}{RC} = 300kHz$. 100pF capacitor is utilized for C, and a $100K\Omega$ analog potentiometer (i.e. variable resistor) is utilized in place of R to give the user the ability to tune the instrument and match the receiver's filter (discussed in the next section). The transmitter's carrier pulse is combined with a message coming from a processing board (as shown in Figure 2.12) via an AND gate and utilizing the AND gate's output signal to drive the LED source via a MOSFET.

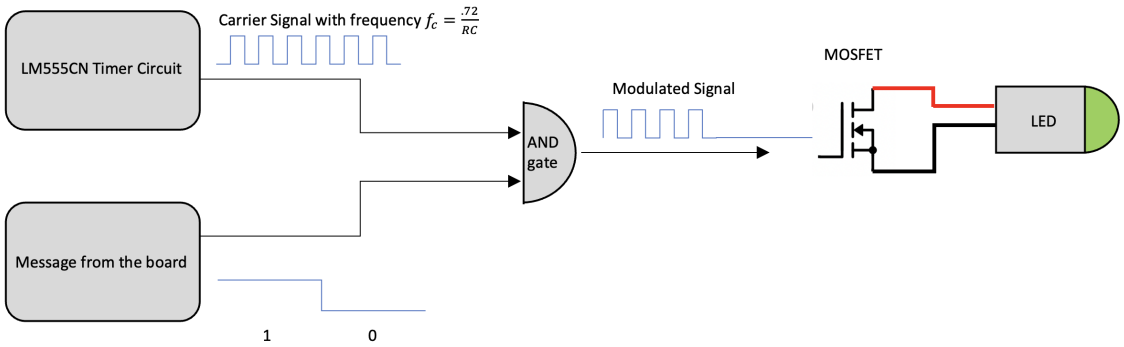

Figure 2.12: Transmitter diagram

The final transmitter circuit diagram is shown in Figure 2.13, and a corresponding Printed Circuit Board (PCB) is shown in Figure 2.14. A Teensy 4.0 board equipped with a 600MHz ARM Cortex-M7 processor is utilized to compile and send message traffic [25].

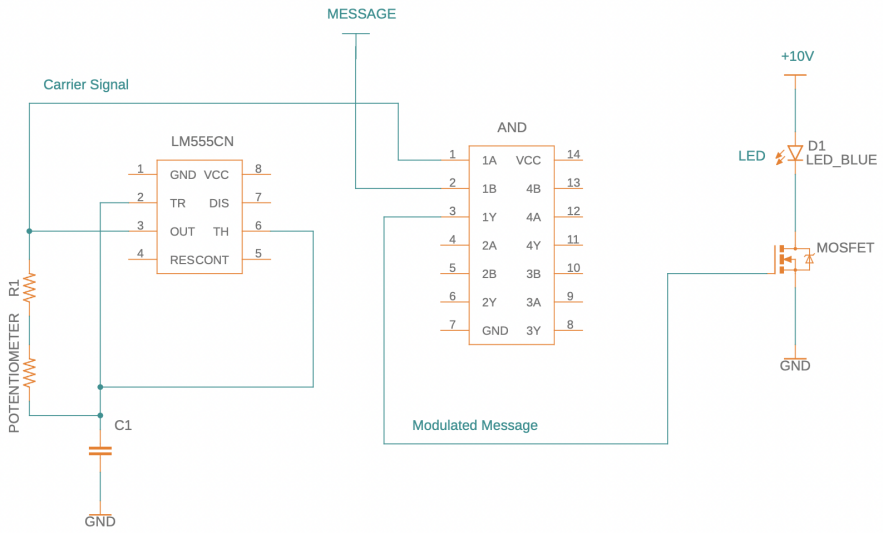

Figure 2.13: Transmitter circuit diagram

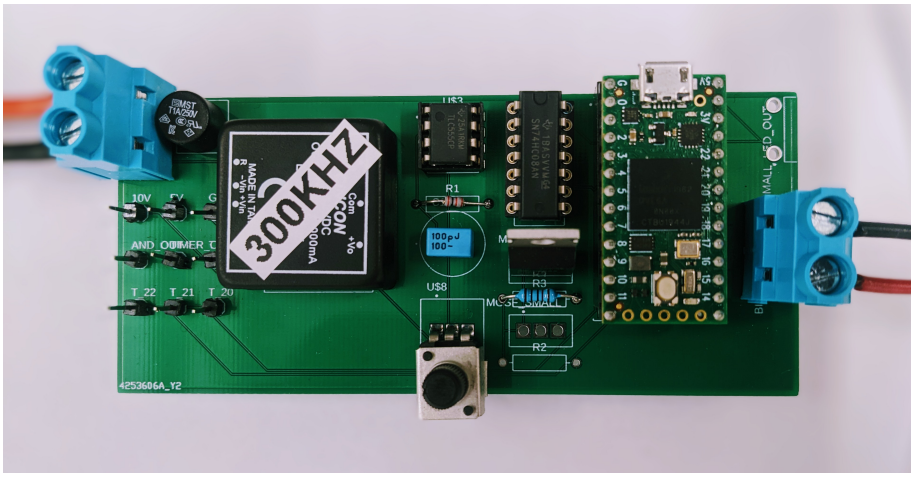

Figure 2.14: Transmitter circuit board

CHAPTER 3

Underwater Receiver Design

3.1 Introduction to Photodiodes

Photodiodes are semiconductor devices with a P-N junction capable of converting light (photons) into electric current [23]. The P-layer contains an abundance of holes (positively charged) while the N-layer contains an abundance of electrons (negatively charged). A depletion region is formed between these two layers with no existing free carriers, and an electric field is created by a separate voltage source [23]. Current flow is induced when light (photons) strike the area at or near the depletion region and form electron-hole pairs, which then travel to P and N layers generating photocurrent [26]. A figure of a typical P-N photodiode cross section is shown on Figure 3.1.

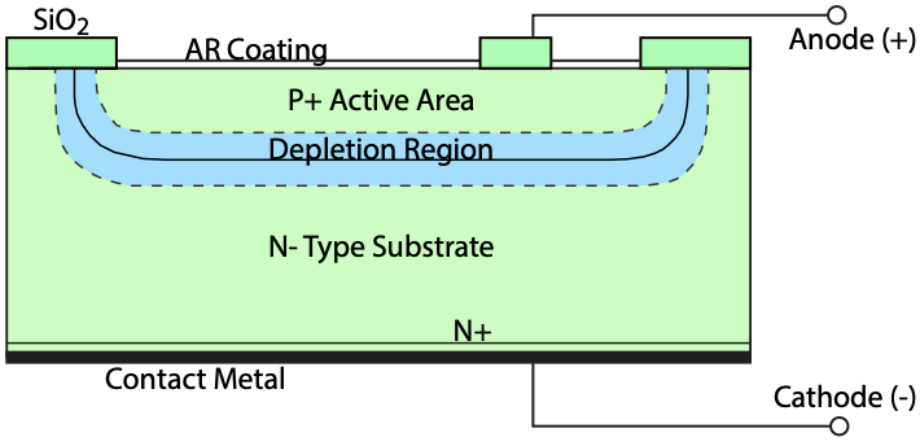

Figure 3.1: Cross section diagram of a P-N photodiode [23]

If electron-hole pairs are formed away from the depletion region, they recombine to create heat. The boundaries at the depletion region act as parallel capacitor plates. The actual

capacitance is determined by the region's width and bias voltage applied to the photodiode [23].

There are four main characteristics that define a photodiode:

- Performance - time necessary for charged carriers to cross the depletion region. This characteristic is determined by the P-N junction capacitance and determines photodiode's response time and speed [23].

- Responsivity - photodiode's ability to induce current for a specific wavelength of light. Within a photodiode, photons release carriers in semiconductor over a range of depths proportional to photon wavelengths [26]. Responsivity is measured in Amps per watt (A/W).

- Dark Current - current induced when there is no incident light present. Dark current is one of the main sources of noise within photodiode electronics [23]. Their levels are lowest in unbiased modes (discussed below) and typically increase with temperature [23].

- Breakdown Voltage - maximum reverse voltage that can be applied across a photodiode. This voltage level typically decreases with increased ambient temperatures and mainly depends on materials used for the construction of the diode (e.g. silicon, germanium, indium, gallium...etc) [23].

There are three main types of photodiodes in today's industry: P-N Junction, PIN, and Avalanche [26]. P-N Junction photodiodes are the most basic type of photodiodes (shown on Figure 3.1). PIN photodiodes are similar to that of P-N Junction diodes but have an additional intrinsic layer added between the two doped layers to prevent unintentional material adulteration. This additional intrinsic layer is highly resistive and increases the electric field strength of a photodiode. As a result, PIN diodes offer decreased junction capacitance values, increased speed and performance, and better quantum efficiency [23]. Additionally,

intrinsic layer increases the spectral range of response by expanding the depletion region [26]. A diagram of a typical PIN photodiode is shown in Figure 3.2.

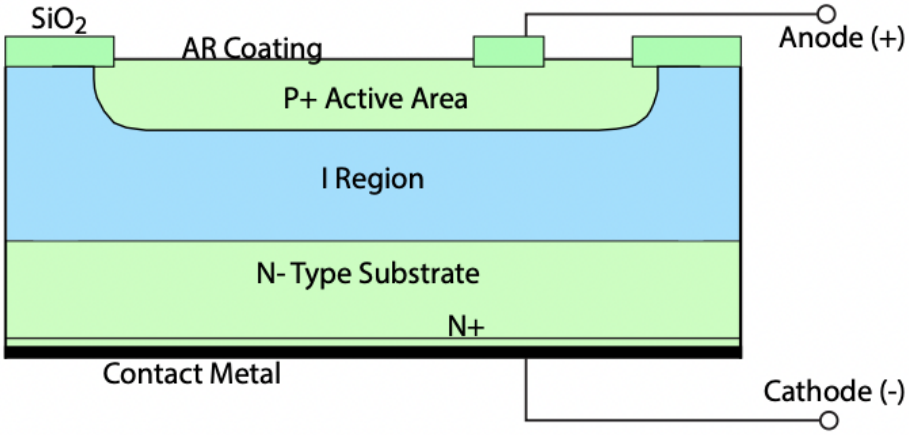

Figure 3.2: Cross section diagram of a PIN photodiode. [23]

Avalanche PhotoDiodes (APD) utilize impact ionization (avalanche effect) to create internal gain in the material [23]. APDs are biased near the breakdown voltage which introduces the avalanche multiplication (gain) to amplify the fundamental photodiode current. This feature enables measurable signals in settings with very low light levels [26]. Although APD current noise levels are typically high due to internal gain, the overall Signal-to-Noise Ratio (SNR) found in APD is typcally higher than that found in PIN and P-N Junction photodiodes [23]. There are two main setbacks found in APDs: difficult bias requirements (bias voltages range 100-400V [27]) and high cost starting with over $100 per unit and going over $1,000 with increasing active area sizes [28]. Figure 3.3 shows a diagram of an APD.

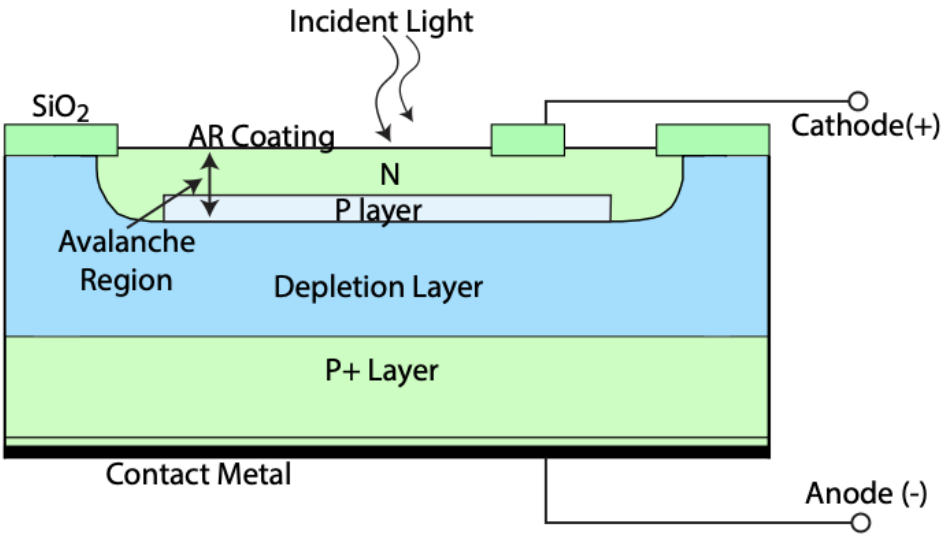

Figure 3.3: Cross section diagram of an APD photodiode. [23]

Another important point of discussion is the typical modes of operation of photodiodes. There are two main modes: (1) Unbiased and (2) Photocunductive.

Unbiased mode occurs when there is no voltage applied across the photodiode. This mode only applies to P-N and PIN diodes. Unbiased mode offers lower dark currents (near zero) and is considered to be the best mode for low light level applications (for PIN and P-N diodes) [23]. Additionally, unbiased mode hinders variations of photocurrent responsivity with temperature changes [23]. A downfall of unbiased operation is the presence of high capacitance due a to narrow depletion region, which in turn degrades speed and performance [29].

Photoconductive mode occurs with the application of a reverse-biased voltage to the photodiode. This voltage causes attraction between the electrons and the positive terminal and between the holes and the negative terminal, thus, further increasing the width of depletion region. A larger depletion area is capable of absorbing more photons which, in turn, decreases capacitance and improves speed and response times [23]. Dark currents actually increase with applied reverse-biased voltage.

Figure 3.4 shows a curve of photocurrent and dark current values for different operating

modes and varying light levels.

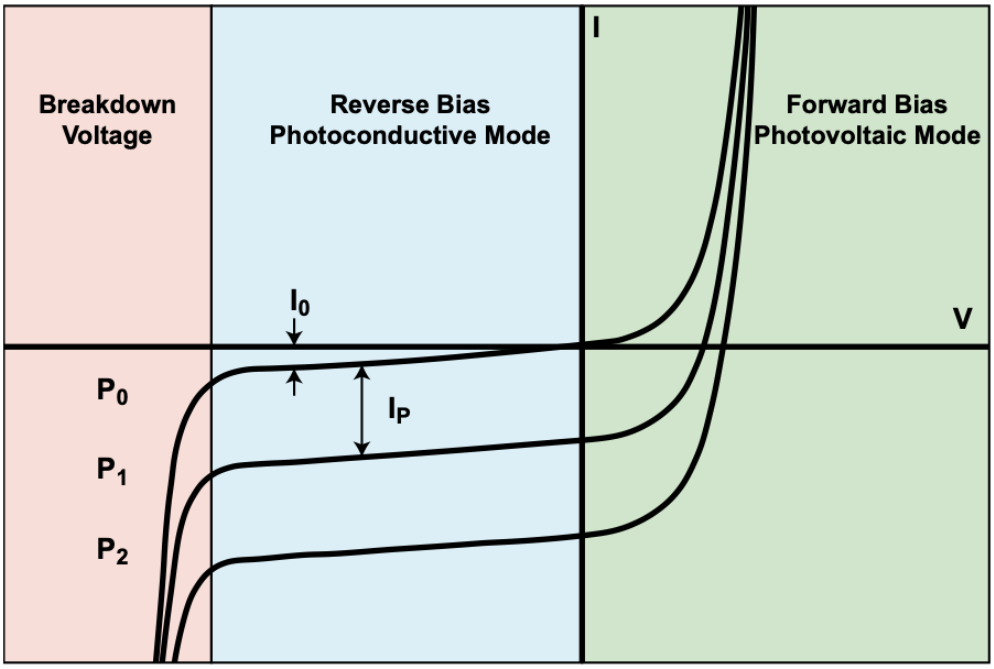

Figure 3.4: I-V Curve of Photodiodes - I_0 (Dark Current), I_p (photocurrent), P (P_i, $i = 0, 1, 2$) showing current at varying light levels with (P_0 denoting no-incident light) [23]

Based on aforementioned information presented an appropriate photodiode is selected to receive optical communication signals and to enable practical communication between receiver and transmitter. APDs are considered and analyzed. They offer very strong responsivity ranging 10-20 A/W for the transmitter spectra (as discussed in Chapter 2). Figure 3.5 shows a spectral response curve for Hamamatsu APDs [27].

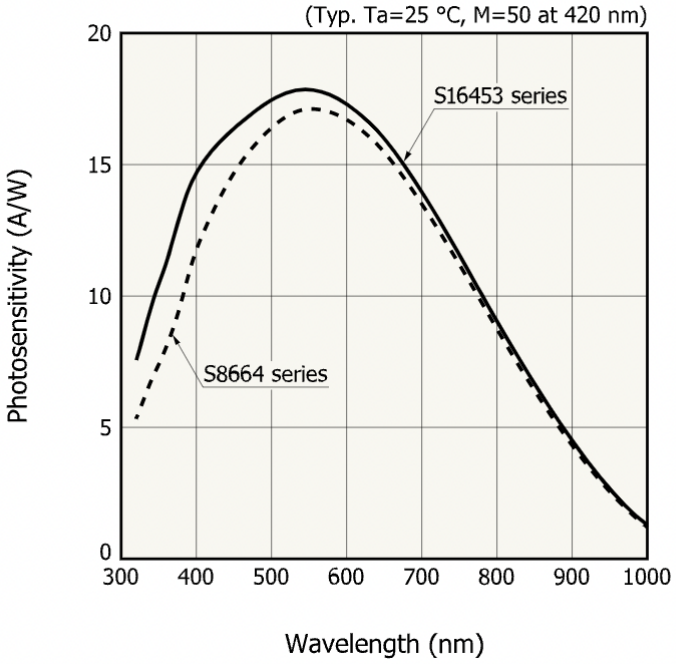

Figure 3.5: Spectral response of Hamamatsu APDs) [27]

Most commercially available APDs offer small active areas ranging between $0.8mm^2$ and $20mm^2$ and cost \$120 to \$660, respectively [28]. Additionally, their biasing requires large near-breakdown voltages (100V to 400V [27]), which are not practical for small UUVs. Therefore, PIN photodiodes are deemed as a better option for this scenario and are, therefore, investigated for this research. and the market is analyzed for final selection. The PS100-6b THD photodiode is selected. Figures 3.6 and 3.7 show part details and spectral response curve.

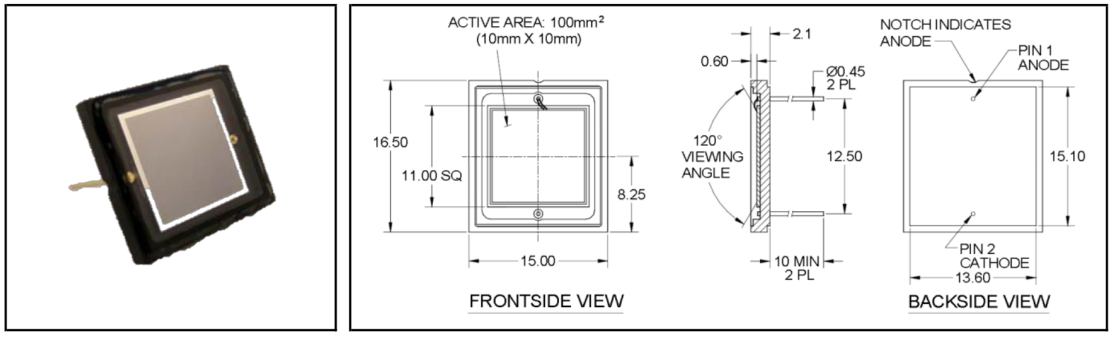

Figure 3.6: First Sensor PS100-6b THD PIN photodiode [30]

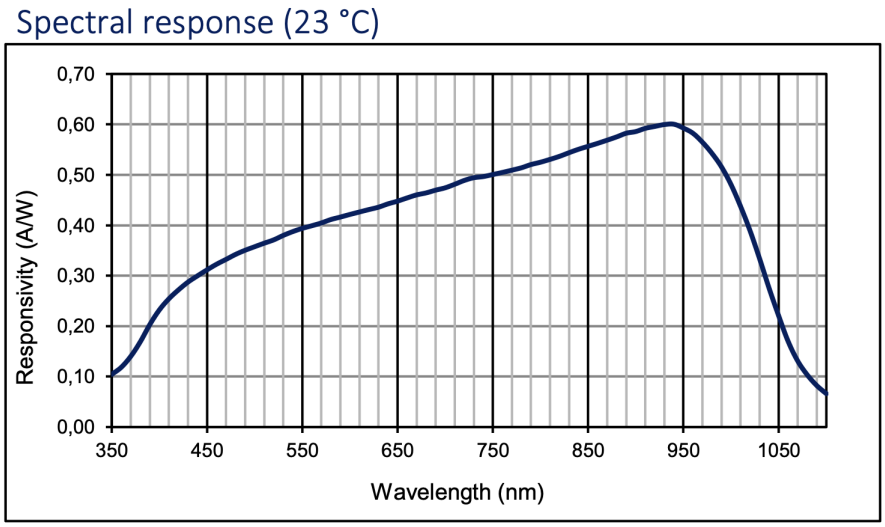

Figure 3.7: PS100-6b spectral response [30]

For a price of $55 per unit, this photodiode offers a large $100mm^2$ active area with the following spectral responses in colors of interest:

- Green ($\lambda = 520nm$) - 0.38 A/W
- Blue ($\lambda = 470nm$) - 0.33 A/W
- Violet ($\lambda = 400nm$) - 0.23 A/W

Even though APD spectral response numbers are much higher, low cost, larger active area and short range requirements deem this photodiode as the best option. Unbiased operation mode is chosen to minimize dark currents and enhance communication ranges.

Photodiodes are prone to noise due to ambient light and can, therefore, be challenging to utilize near the water surface or in other well-lit areas [31]. In order to minimize the ambient noise and enhance receiver's SNR, a set of optic bandpass filters is utilized for the wavelengths of interest. Edmund Optics Hard Coated OD 4.0 50nm bandpass filters are selected with the following specifications:

- Violet - $\lambda_c = 400nm$

- Blue - $\lambda_c = 475nm$
- Green - $\lambda_c = 525nm$

Filter center wavelengths are selected to match LED specifications (Figure 2.4) with the largest bandwidth available. Figure 3.8 shows a transmission curve for the green color (525nm) filter.

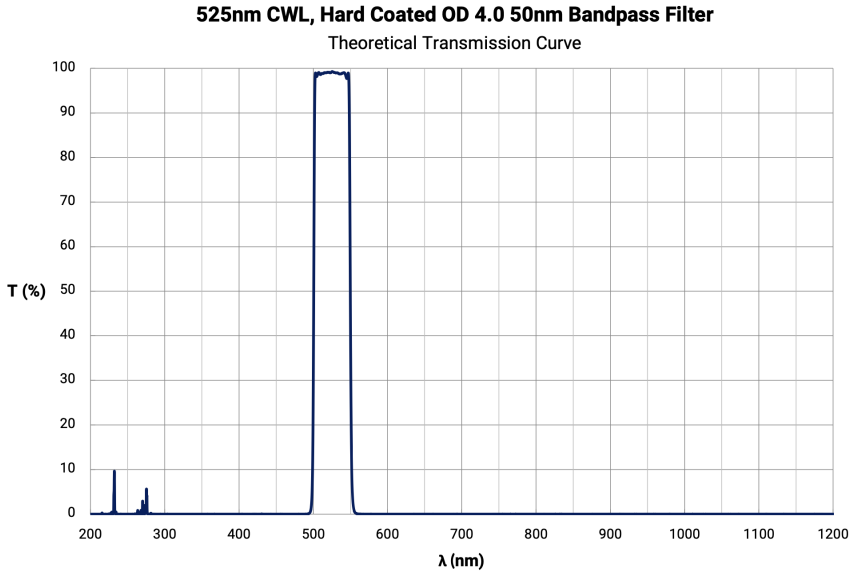

Figure 3.8: Edmund Optics BPF Transmission Curve for $BW = 50nm$ and $\lambda_c = 525nm$ [32]

3.2 Receiver Circuit Design

In order to efficiently convert PIN sensor's photocurrent into a readable voltage, a transimpedance amplifier method is chosen, where an operational amplifier is utilized to convert current to voltage while buffering the rest of the circuit [33].

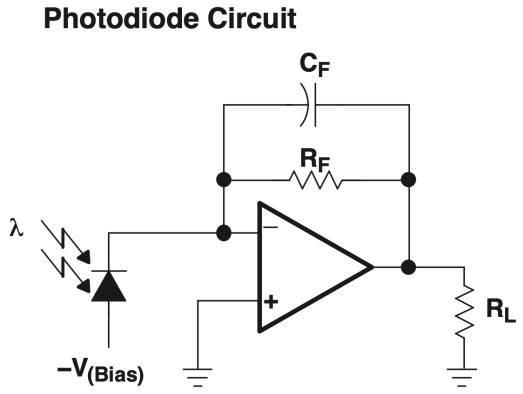

Figure 3.9: Photodiode Transimpedance Amplifier [34]

Figure 3.9 above demonstrates a generic photodiode transimpedance circuit, where a signal voltage V_{out} is generated across R_L based on the amount of current produced by a photodiode:

$$V_{out} = I_D Z_F \tag{3.1}$$

Where I_D represents the amount of generated photocurrent (A), and Z_F represents a total feedback impedance due to the feedback resistor R_F and the feedback capacitor C_F. In general, operational amplifiers (op-amps) can be described as "gain engines" for negative feedback with single-ended output and extraordinarily high gain [33]. Op-amps are a starting point of most analog circuits included in amplifiers, current sources, integrators, filters, regulators, current-to-voltage converters, etc. [33]. They have two inputs: non-inverting input (+) and inverting input (-), the difference between which dictates its output. The output is positive if the non-inverting input is greater and vice versa. Op-amps inherently have a very large internal gain and are almost never used without feedback [33]. To ensure fast operations and excess bandwidth available, the Texas Instruments THS4631 operational amplifier is chosen for this implementation. The THS4631 offers a large Gain BandWidth (GBW) product of 210MHz, and a fast slew rate of $1000V/\mu s$. Furthermore, its low current

and voltage noise levels allow for amplification of significantly low amplitude input signals while still maintaining a large signal-to-noise ratio [34]. These key characteristics make the THS4631 an ideal option for a photodiode transimpedance amplifier. To ensure stability and prevent excessive/additional oscillations and ringing, a small 10pF feedback capacitor C_F is placed in parallel with the feedback resistor R_F to balance the photodiode's large inherent capacitance. Due to its large active area, the PS100-6b photodiode has a capacitance of 720pF in unbiased operation [30]. Typically, there are three main capacitance sources in a transimpedance network. The total input capacitance, C_{in}, is determined as

$$C_{in} = C_D + C_A + C_W \tag{3.2}$$

Where C_D represents photodiode capacitance, C_A represents operational amplifier's capacitance, and C_W represents wiring capacitance. In this circuit design, the photodiode's main source of capacitance, C_D, is orders of magnitude higher than that of C_A (3.9pF [34]). Wiring capacitance is also assumed to be negligible in comparison to C_D. Therefore, C_{in} can be approximated such that $C_{in} = C_D = 720pF$. Detector's capacitance combined with the feedback resistor forms a low-pass filter with a cutoff frequency (in HZ)

$$f_{R_F C_{in}} = \frac{1}{2\pi R_F C_{in}} \tag{3.3}$$

Where $f_{R_F C_{in}}$ represents the low-pass filter's 3dB breakpoint (i.e. break frequency), which results in lagging phase shift at higher frequencies. When combined with op-amp's own phase shift, the additional phase lag can produce oscillations [35].

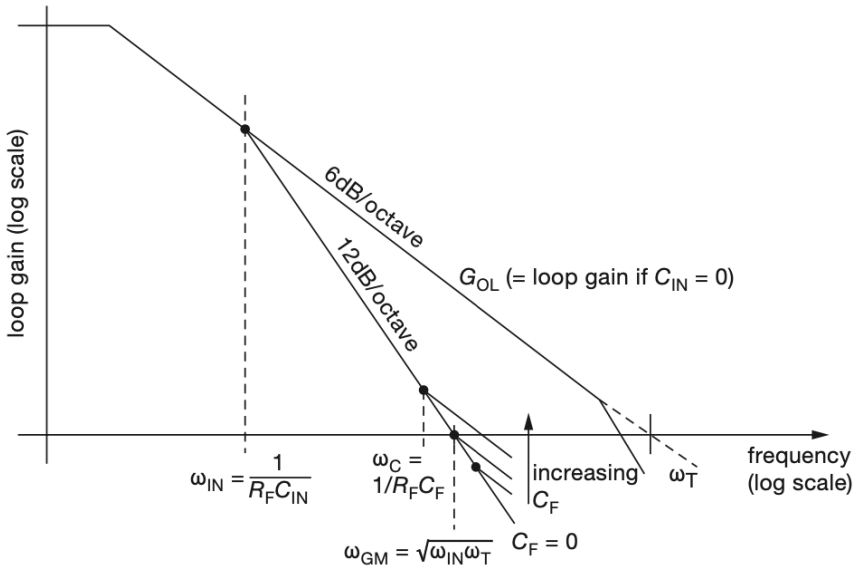

Figure 3.10: Magnitude portion of frequency response (in dB) of the transresistance amplifier. Stability requiring the closed-loop gain curve to intercept the unity-gain axis at a6 dB/octave slope [35]

Feedback capacitor C_F is chosen in accordance with the Bode plot shown in Figure 3.10. The photodiode's C_D stops 6dB/Octave rolloff of feedback network at $f_{R_F C_{in}}$, and capacitance size is chosen so that resulting closed-loop gain reverts safely back to a 6dB/octave slope before reaching the unity gain axis [35]. Unstabilized amplifier reaches unity gain at a frequency located halfway between $f_{R_F C_{in}}$ and f_T, where f_T represents the op-amp's GBW. This mid-point is known as the "geometric mean frequency" and may be calculated as

$$f_{GM} = \sqrt{f_{R_F C_{in}} f_T} \tag{3.4}$$

Where f_{GM} represents the geometric mean frequency [35]. Based on Hill's The Art of Electronics, a good "rule of thumb" for selecting a feedback capacitor is to maintain the resulting $R_F C_F$ cutoff frequency at about 70% of f_{GM} such that

$$f_C = \frac{1}{2\pi R_f C_f} = \sqrt{\frac{f_{R_F C_{in}} f_T}{2}} \tag{3.5}$$

Where f_C represents the cutoff frequency (in Hz) of the low-pass filter resulting from the total feedback impedance [35]. f_C and the resulting feedback capacitance are calculated for this design with the following selected values:

- $C_{in} = C_D = 720pF$
- $R_F = 10k\Omega$: this value is chosen small enough to maintain adequate bandwidth (details shown below) and large enough to maintain adequate SNR while detecting photocurrent at lower levels (i.e. longer ranges).
- $f_T = 210MHz$ (GBW for THS4631 op-amp) [34]

$f_{R_F C_{in}}$ is calculated

$$f_{R_F C_{in}} = \frac{1}{2\pi \cdot 10,000 \cdot 720 \times 10^{-12}} = 22.104kHz \tag{3.6}$$

f_{GM} is calculated as

$$f_{GM} = \sqrt{f_{R_F C_{in}} f_T} = \sqrt{22.104kHz \times 210MHz} = 2.15 \times 10^6 Hz \tag{3.7}$$

C_f can then be calculated per aforementioned "rule of thumb" and Equation 3.5 such that

$$C_f = \frac{1}{2\pi R_f \cdot 0.70 f_{GM}} = \frac{1}{2\pi \cdot 10,000 \cdot 0.70 \cdot 2.15 \times 10^6} = 1.06 \times 10^{-11} F \approx 10pF \tag{3.8}$$

An alternative way of analyzing C_F effects on transimpedance amplifier's stability is by comparing the effective damping ratio ζ (assuming a second order response), where $f_C = 0.7 f_{GM}$ results in slightly under damped system (i.e. $\zeta = 1$) the quickest response without excessive oscillations [35]. Figure 3.11 illustrates a visual example of underdamped, critically damped and overdamped amplifier responses.

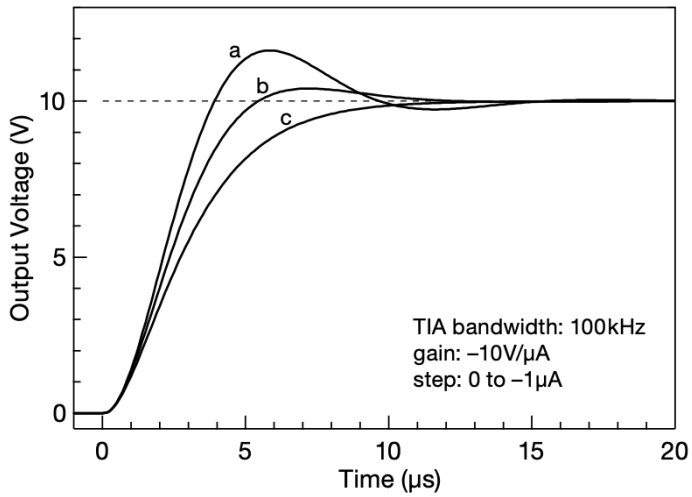

Figure 3.11: Transimpedance amplifier step response example for three choices of C_f corresponding to characteristic frequencies $f_C = 0.7 f_{GM}/\zeta$, with the damping ratio ζ equal to (a) more underdamped, (b) slightly underdamped, and (c) overdamped. [35]

In order to further enhance signal amplitude, the transimpedance amplifier's output is fed into another op-amp circuit with a gain of 10. The resulting circuit diagram is shown in Figure 3.12, where $R1 = 10k\Omega, C1 = 10pF, R2 = 1k\Omega, R3 = 10k\Omega$. $R1$ value is chosen to maintain adequate TIA bandwidth to accommodate signals at $f_C = 300kHz$ and provide a readable signal. $R2$, and $R3$, values are sized to produce a large enough gain to enable longer ranges, but small enough to avoid a large noise floor. These values are selected experimentally, where post-filter noise floor (discussed below) remains $< 200mV$.

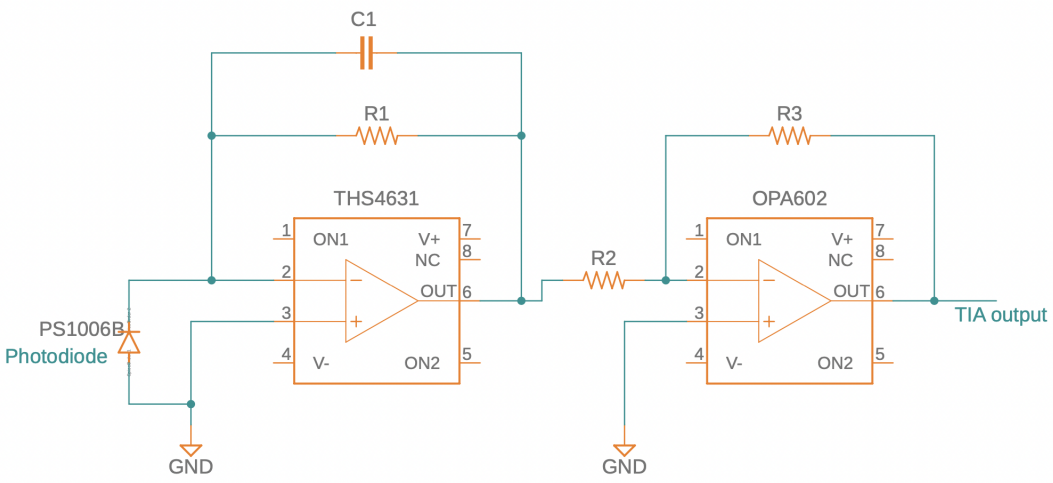

Figure 3.12: Resulting transimpedance amplifier circuit diagram

A bandpass filter is designed and constructed in order to distinguish messages with transmitter's carrier frequency f_c and to also filter (high-frequency) ambient noise. An active filter design is selected, where the op-amps act as an "active" circuit and provides buffers between circuit stages (i.e., prevent interaction between circuit subsystems) [36]. A Multiple Feedback BandPass (MFBP) circuit is selected and analyzed (shown in Figure 3.13).

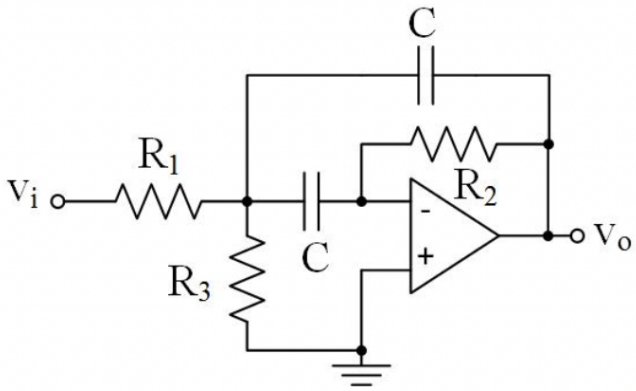

Figure 3.13: Multiple feedback bandpass circuit [37]

MFBP is one of the simplest and most useful bandpass filter variations used in analog electronics [36] and has the following characteristics:

- Q is limited to 20, where Q represents filter's ratio of carrier frequency to bandwidth ($Q = f_c/BW$)

- MFBP performance largely depends on the op-amp's bandwidth (GBW restricted to being greater than $2Q^2 f_c$) [36]
- Capacitor tolerances of 5% or less and resistor tolerances of 1% are required.
- MFBP bandwidth is determined by $R2$ and C values and is invariant of $R1$ and $R3$ values [36]

$$BW = \frac{1}{\pi R_2 C} \tag{3.9}$$

- Resonant frequency, f_R, is defined by

$$f_R = \frac{1}{2\pi C}\sqrt{\frac{R_1 + R_2}{R_1 R_2 R_3}} \tag{3.10}$$

- Q is defined by

$$Q = \frac{1}{2}\sqrt{\frac{R_3}{R_2}} \times \sqrt{\frac{R_1}{R_1 + R_2}} \tag{3.11}$$

Instead of calculating resistor and capacitor values manually, a Texas Instruments Filter Design tool is utilized in order to achieve the most optimal results for the filter's noise reduction and output performance. A two-stage, fourth-order narrowband Butterworth design is generated and is shown in Figure 3.14, and [from Pg.36]. The filter's magnitude and phase responses are shown in Figure 3.15.

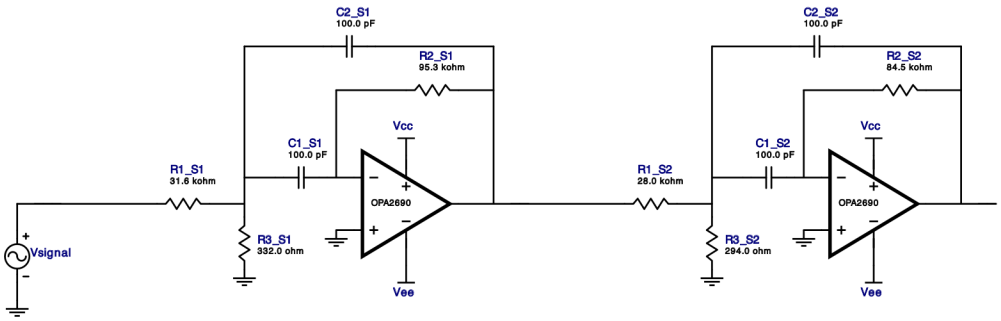

Figure 3.14: 4^{th} order two-stage Butterworth bandpass filter with $f_C = 300kHz$ [38]

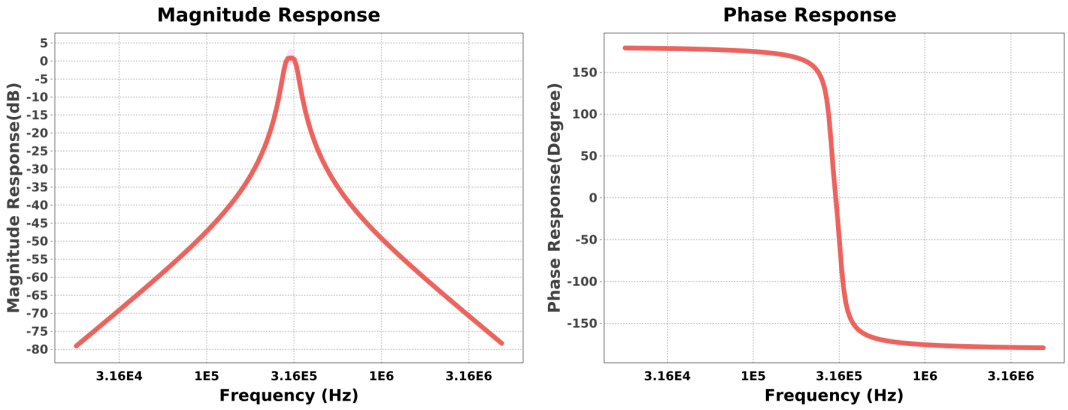

Figure 3.15: Calculated filter magnitude (left) and phase response (right) [38]

The bandpass filter has the following characteristics:

- $f_C = 300kHz$, where $f_{CS1} = 284kHz$ and $f_{CS2} = 321kHz$
- BW = 50kHz, with -3dB break frequencies of $f_L = 275kHz$ and $f_U = 325kHz$
- Q = 6, where $Q_1 = 8.516$ and $Q_2 = 8.521$
- Overall filter gain $G_{filter} = 1.122$

All resistors and capacitors selected for this filter are within 1% tolerance or greater. Even though Texas Instruments OPA2690 op-amp is recommended in the design, OPA2889 is utilized in its place due to component availability. OPA2889 offers a GBW of 75MHz,

which is sufficient for this design:

$$GBW_{min} = 2Q^2 f_c = 2 \cdot 6^2 \cdot 300,000 = 21.6MHz < 75MHz \tag{3.12}$$

One major lesson learned during filter design stage is to properly choose an appropriate carrier frequency to the desired bit rate, where $\frac{bit\,rate}{f_C} \leq \frac{1}{20}$ should be maintained for optimal performance. Figures 3.16 through 3.18 demonstrate the effects of varying carrier frequencies.

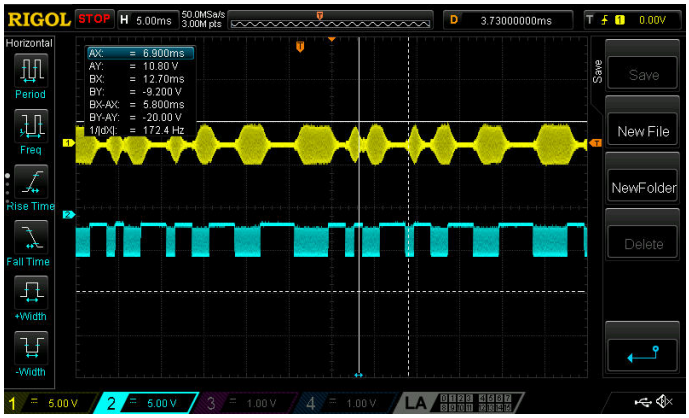

Figure 3.16: filter output (yellow) at $f_C = 10kHz$ and input signal at bit rate of 1 kbps (blue)

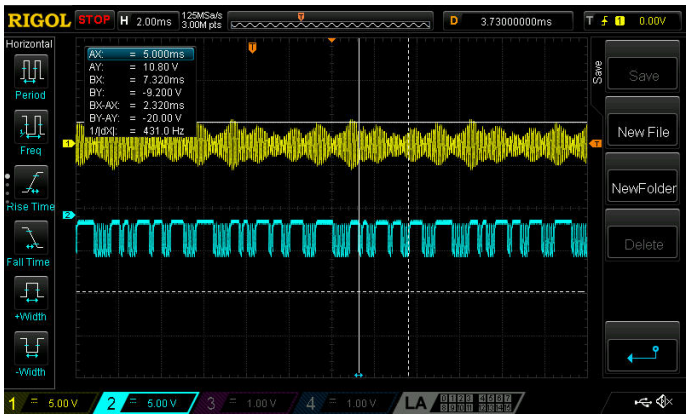

Figure 3.17: filter output (yellow) at $f_C = 10kHz$ and input signal at bit rate of 5 kbps (blue)

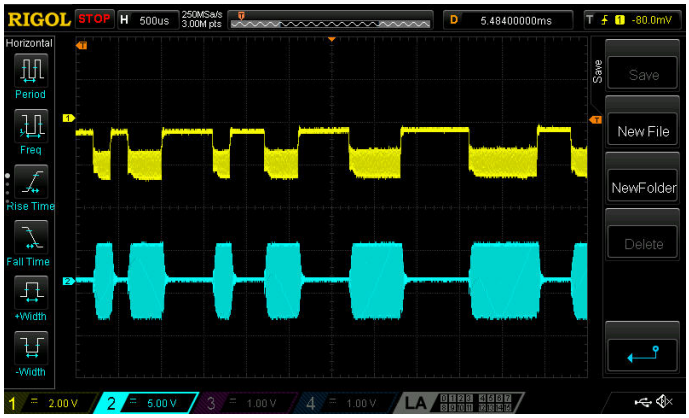

Figure 3.18: filter output (blue) at $f_C = 100kHz$ and input signal at bit rate of 5 kbps (yellow)

10kHz and 1 kbps filter output demonstrates a slight slope (Figure 3.15), which affects signal interpretation during the analog-to-digital phase (width of bits varying with signal strength). When bit rate is increased to 5kbps with the same carrier frequency (Figure 3.16), the filter's output is no longer readable (two iterations of a carrier wave per bit is not enough to trigger an accurate filter output). When the carrier frequency is increased to 100kHz (with the same bit rate of 5 kbps) (Figure 3.17), this results in a cleaner filter output and matches the bit width and timing of that of the input signal. A carrier frequency of 300kHz is therefore selected for this research and 5 kbps bit-rate is maintained to provide sufficient room during filtering stage.

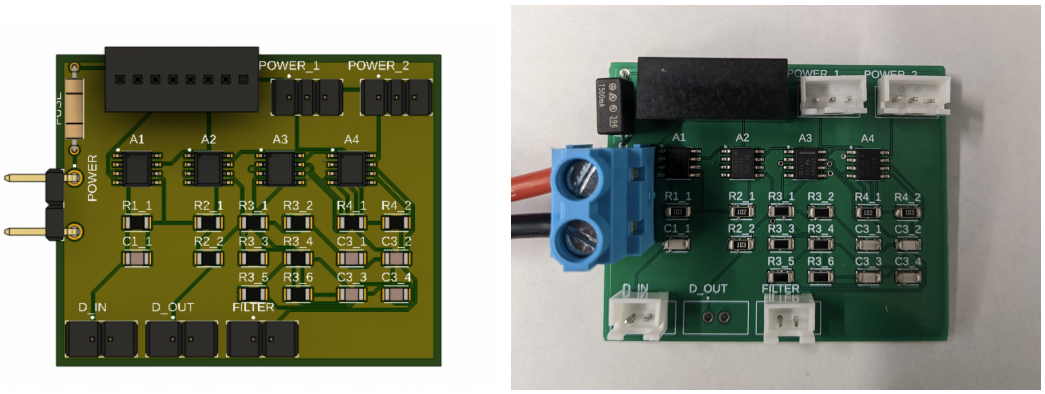

Figure 3.19: Analog stage CAD design (left) and printed circuit board (right)

Following the filtering stage of the receiver circuit, an additional op-amp with a gain of

10 is added to the circuit to amplify the analog output and enable longer communication ranges. The final analog design and circuit board are shown in the Figure 3.19 above.

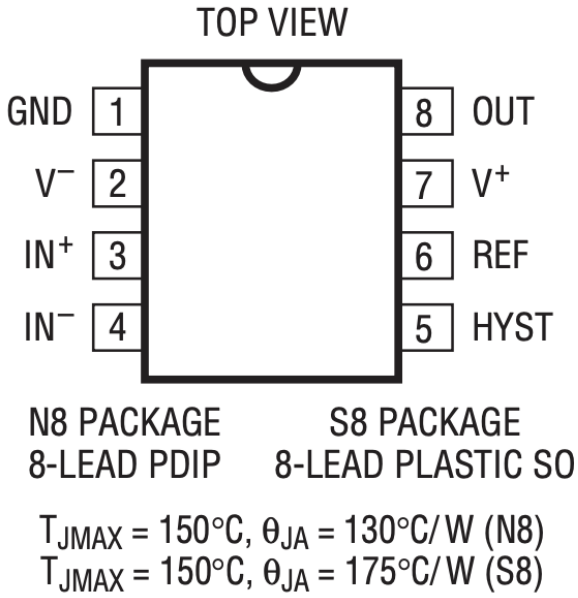

Figure 3.20: LTC-1440 single comparator pinout diagram [39]

The analog-to-digital conversion circuit is designed next, where the analog output signal is transformed into a digital form via a comparator. Figure 3.20 shows a pinpout diagram for LTC-1440 chip. Comparators provide an important interface between analog input signals and the digital domain [40]. Comparators enable 1-bit analog-to-digital conversion and resemble a pinout similar to that of Operational Amplifiers. The comparator's output goes to a higher level signal ("high") when non-inverting (+) terminal is greater than that of the inverting (-) terminal and stays at a low level ("low") otherwise [40]. A distinct benefit of comparators is the fact that they do not saturate when operating without feedback [40]. In this design, the filter's output is fed into the non-inverting terminal of the LTC-1440 comparator, while an external reference voltage is fed into the inverting terminal. Although the LTC-1440 offers a reference voltage of 1.17V above the negative saturation voltage, this reference voltage is too large to enable digital output signals to be triggered at far ranges (200mV-400mV). An adjustable reference voltage is created due to the analog signal's small

noise floor variations with signal strength and ambient environment. The full analog-to-digital circuit of the proposed design is shown in Figure 3.21.

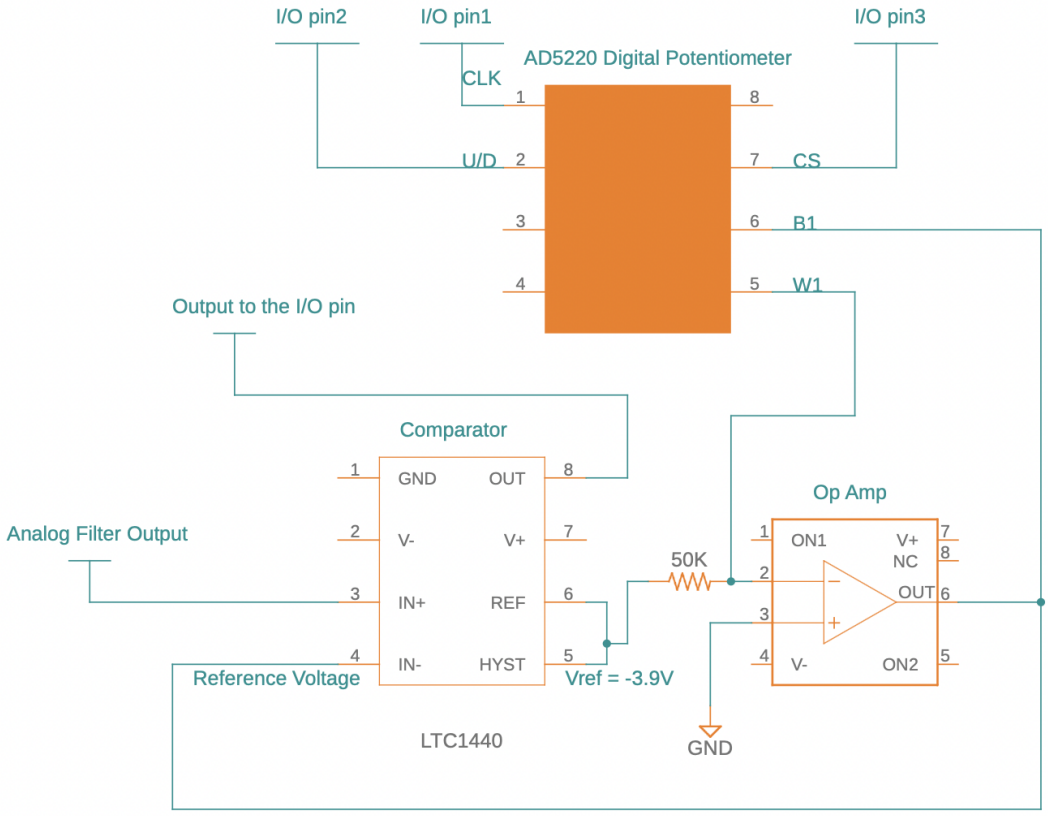

Figure 3.21: Analog-To-Digital circuit diagram

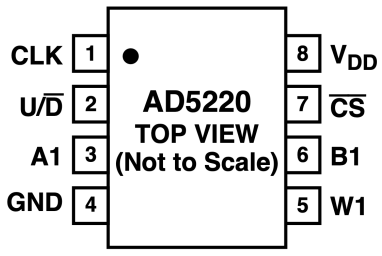

$\overline{CS}$	CLK	U/$\overline{D}$	Operation
L	↓	H	Wiper Increment Toward Terminal A
L	↓	L	Wiper Decrement Toward Terminal B
H	X	X	Wiper Position Fixed

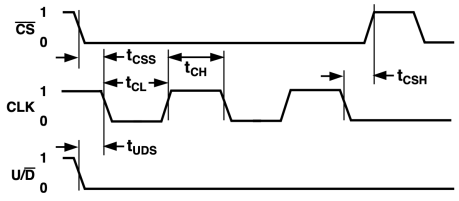

Figure 3.22: AD5220 digital potentiometer pinout diagram and truth table [41]

A reference voltage digital control is designed by taking comparator's available reference voltage and feeding it into an op-amp. The reference voltage is then changed digitally

by manipulating the op-amp's gain via a digital potentiometer, which (in the case of this work) is controlled by a Teensy 4.0 microcontroller. A pinout diagram and truth table shown in Figure 3.22, which describe the control procedures for AD5220 $0 - 100k\Omega$ digital potentiometer. Potentiometer resistance (between B1 and W1 pins) is manipulated by CLK (pin 1), U/D (pin 2) and CS (pin 7). Resistance is increased by one unit per clock's trailing edge if CS-pin is "low" and U/D pin is "high", decreased if CS-pin is "low" and U/D pin is "low," and remains fixed if CS-pin is "high". The output reference voltage becomes the following:

$$V_{ref} = (-5V + 1.17V) \times \frac{-R_{pot}}{50k\Omega} \tag{3.13}$$

Controlling reference voltage with a potentiometer enables small reference voltage V_{ref} adjustments without the need to modify hardware. An example of the comparator's digital output and respective inputs is shown in Figure 3.23.

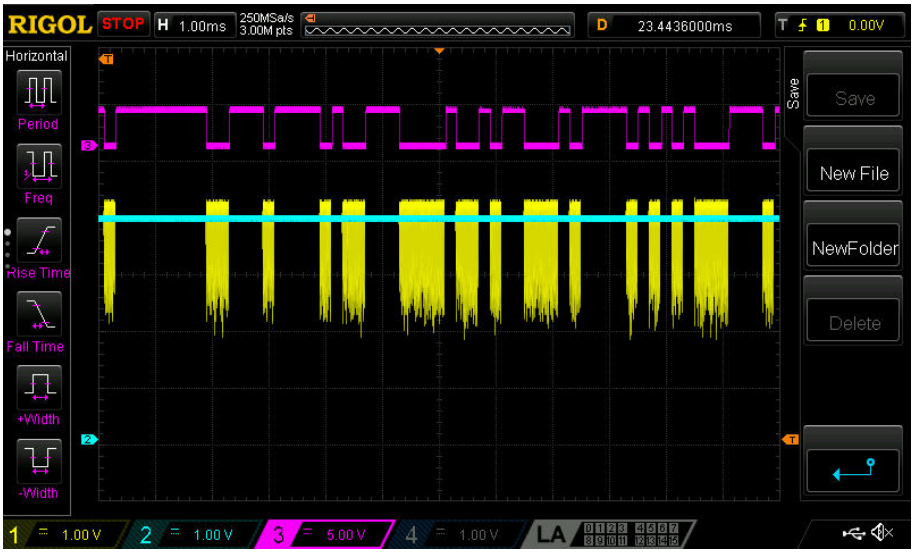

Figure 3.23: Analog input (yellow), adjusted reference voltage (blue), and comparator's digital output (magenta)

One important detail to note is the fact that the analog filter's output (yellow) is inverted prior to inputting its voltage into a comparator. This is achieved by using an additional

operational amplifier's inverting input (OPA-602BP not shown in the circuit diagram) in a comparator configuration, where the non-inverting terminal is grounded and no feedback is passed from the output. This stage is used to remove the filter's negative voltage oscillations and acts in place of a rectifier (Figures 3.15-3.17 show filter outputs ranging from -5V to 5V during binary 1s, while noise floor is maintained approximately at 0 during binary 0s). Even though it is not recommended to use op-amps in configurations with no feedback (including comparator mode) [42], this configuration is, in fact, effective for this research. Once the digital output (magenta signal in Figure 3.23) is available, it is stepped down from 5V to 3.3V (as Teensy 4.0 board pins do not support 5V signals [25]) and fed into the board for digital processing. The final analog-to-digital circuit board is shown in Figure 3.24 and the complete receiver photo is shown in Figure 3.25.

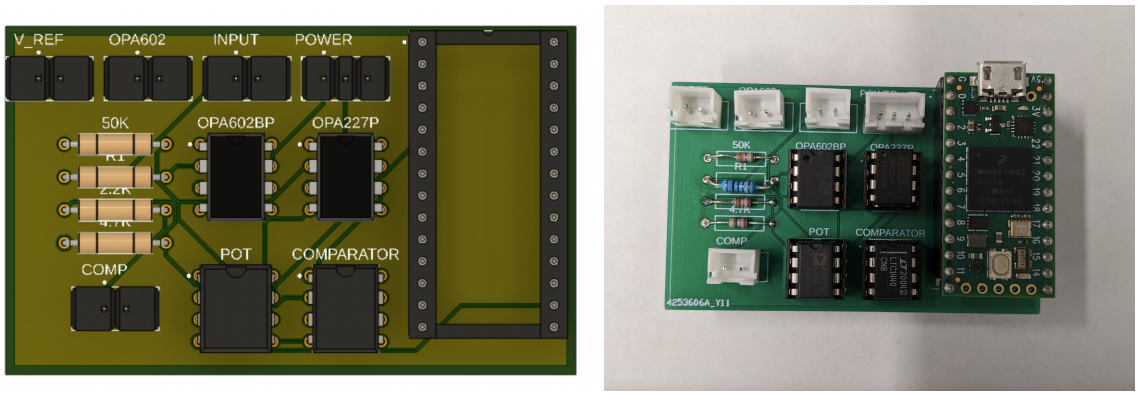

Figure 3.24: A-to-D stage CAD design (left) and printed circuit board (right)

Complete receiver photo is shown in Figure 3.25.

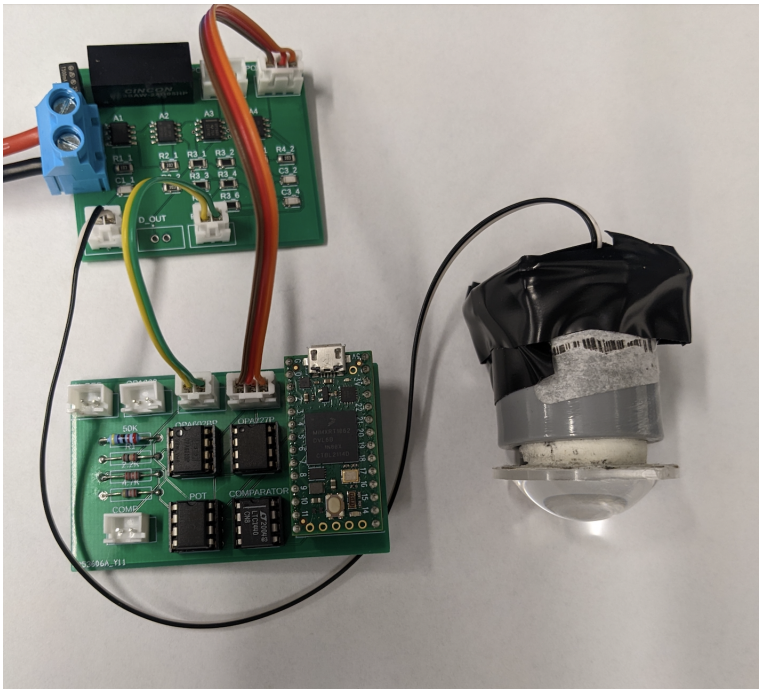

Figure 3.25: Complete optical receiver system

3.3 Projected Received Signal Amplitude Calculation

First, projected light intensity (calculated in Equation 2.6) is used to calculate projected photocurrent at the photodidode sensor such that

$$I_D(\lambda) = DR(\lambda) \times LI \times A_{PD} \tag{3.14}$$

Where $DR(\lambda)$ is the photodiode's responsivity for a given wavelength λ (discussed in Section 3.1), LI is the projected light intensity calculated in Equation (2.6), and A_{PD} is the photodiode's active area ($100mm^2$ in this case). Figure 3.26 shows a projected curve of the received photocurrent for a variety of LEDs of interest to be tested. Although UV photocurrent is projected to be slightly lower than those of blue and green at ranges below 8 meters, its projected values are strong enough to to convert to a readable signal. Photocurrent generated by the blue light is projected to produce signal values slightly higher than those of UV and green (at all ranges).

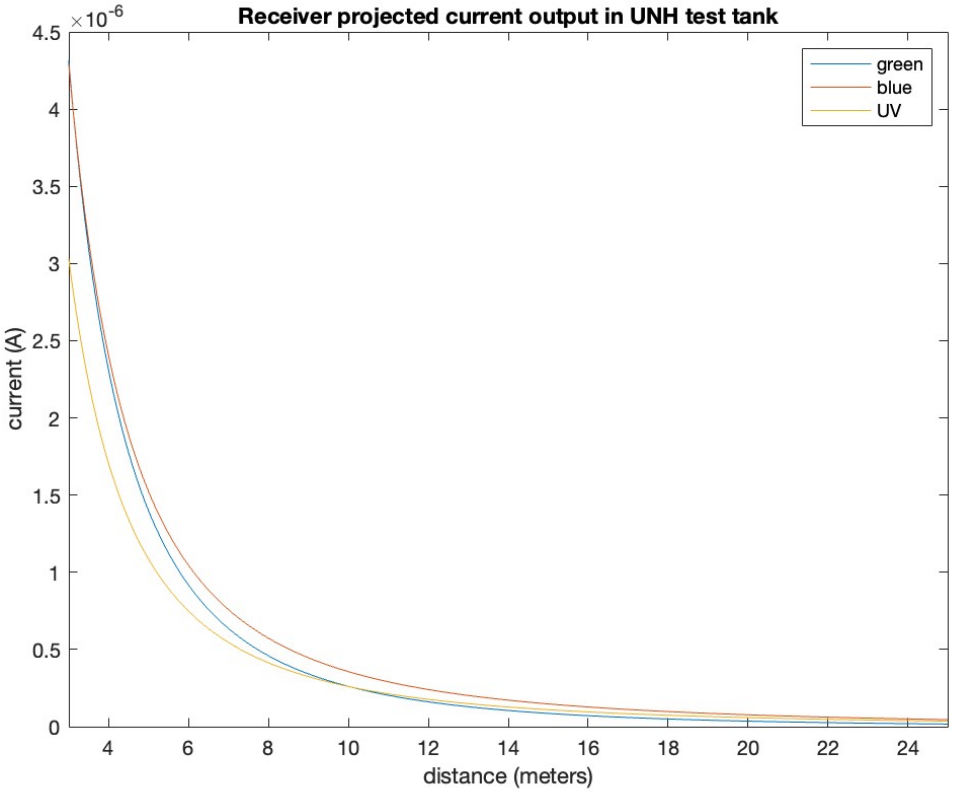

Figure 3.26: Projected photodiode current values

TIA's projected voltage output is calculated next. To measure and compare signal strength of each LED, the transimpedance amplifier stage of the receiver (Figure 3.12) is utilized and slightly modified. $R1$ and C values are kept at $10k\Omega$ and 10pF respectively per calculations in the Equations 3.6 through 3.8. R_3 value is changed for this specific experiment to $196k\Omega$ to maximize incoming signal's gain and to reduce error while reading the values during testing. 10kHz carrier frequency is utilized for this test and bits are sent at 1kbps rate (the original setup prior to investigating and sizing the proper carrier frequency). Due to mostly resistive nature of the TIA's impedance, its capacitance is neglected for estimated calculations as follows:

$$Z_{TIA} = \frac{R_F Z_{C_F}}{R_F + Z_{C_F}} = 9,999.99\angle -0.36^\circ\Omega \approx 10k\Omega \tag{3.15}$$

Where Z_{TIA} represents the transimpedance amplifier's total impedance and Z_{C_F} represents the impedance of the feedback capacitor ($Z_{C_F} = \frac{1}{j\omega C}$). The projected output voltage is calculated such that

$$V_{out} = (I_D R_F)\left(\frac{-R_3}{R_2}\right) \tag{3.16}$$

Where I_D is the projected current, $R_F = 10k\Omega$ is the TIA's impedance (Equation 3.15), $R_2 = 1k\Omega$ and $R_3 = 196k\Omega$. Figure 3.27 shows a graph of the projected output voltage signals for violet (400nm), blue (460-470nm) and green (520-525nm) LED lights. Any value over 5V is assumed to be 5V due to the saturation limit of the op-amps's rail/power supply. Projected voltage signal patterns match photocurrent predictions, where UV signal is projected to be slightly lower at ranges below 8m and blue is projected to produce highest signal values at all ranges.

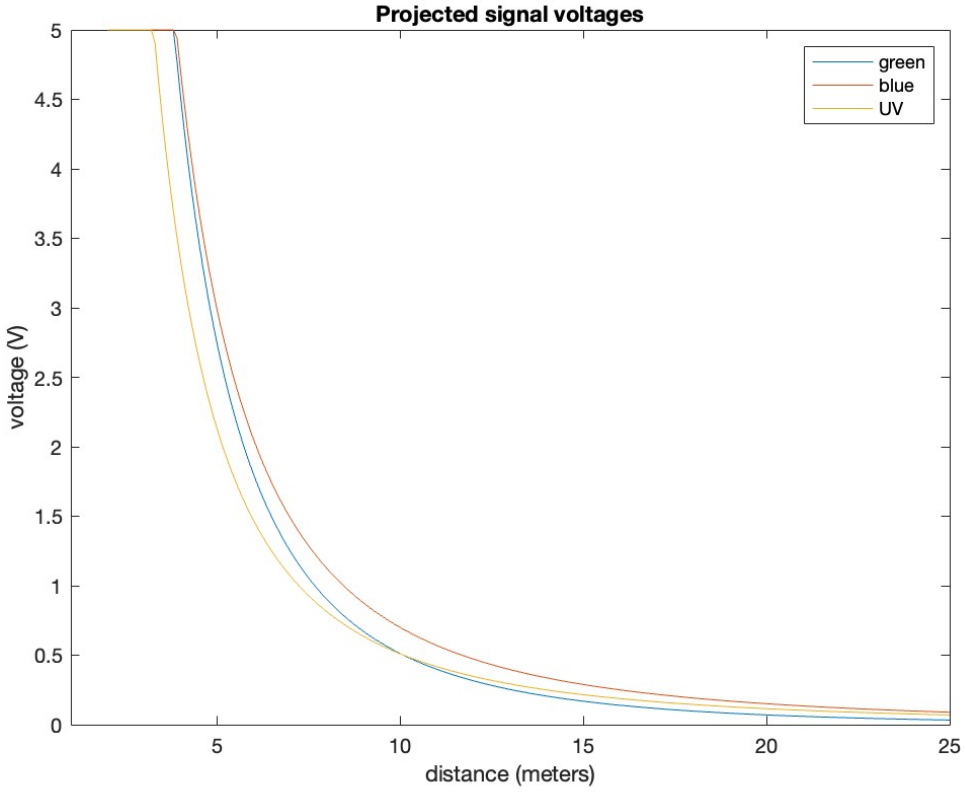

Figure 3.27: Projected voltage output values

CHAPTER 4

Underwater Experimental Tests

4.1 Experiment setup

A series of experiments are conducted in order to test calculated light and signal values. First, the transmitter and receiver are placed into watertight enclosures and tested with a pressure gauge to ensure water integrity. Blue Robotics 4-inch tubes are utilized [43] and a blue robotics tether is connected to the receiver to enable signal measurements. Figure 4.1 shows transmitter and receiver tubes configured for underwater testing.

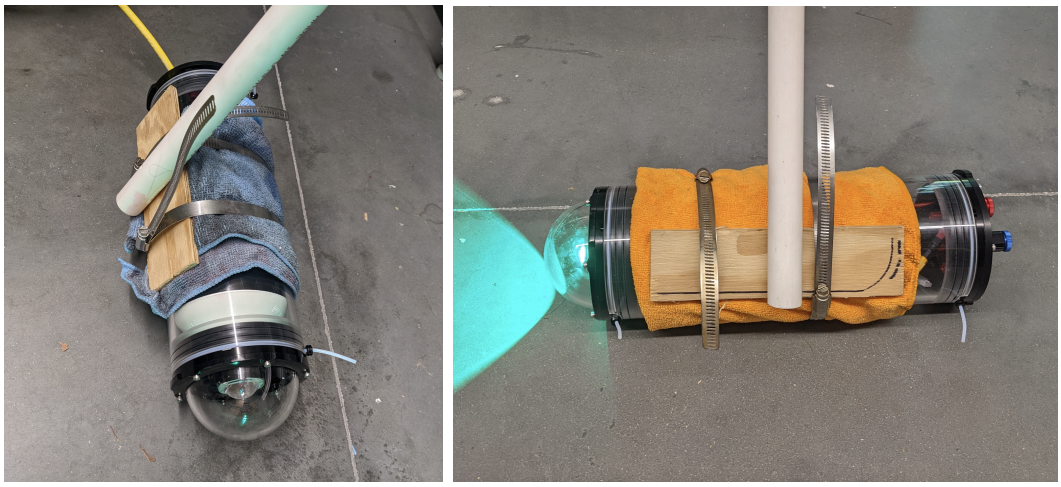

Figure 4.1: Receiver (left) and transmitter (right) tubes prepared for testing

The 60ft x 40ft x 20ft UNH Chase Engineering Tank is utilized for this experiment. Each tube is connected to a 7-foot-long 3/4" PVC pipe, with the top of the pipe tied to a large buoy and the bottom tied to a 5kg ballast weight. Tubes are placed in the water with both transmitter and receiver located roughly eight to nine feet below the water surface. Figure 4.2 shows a photo of a submerged transmitter during testing.

Figure 4.2: Transmitter tube during testing

The transmitter is left disconnected from the user (i.e., tetherless) for the duration of this experiment with a binary message pre-coded into its board: 0010 1100 0100 1100 0111 0000 1111. The message is sent repeatedly for the duration of the experiment. Receiver's tether is connected to the work station (located at the side of the tank) which is utilized to capture data throughout this experiment. A reference rope/line is ran across the tank with 1-meter increments (marked with tape) to track distance between transmitter and receiver (Figure 4.3).

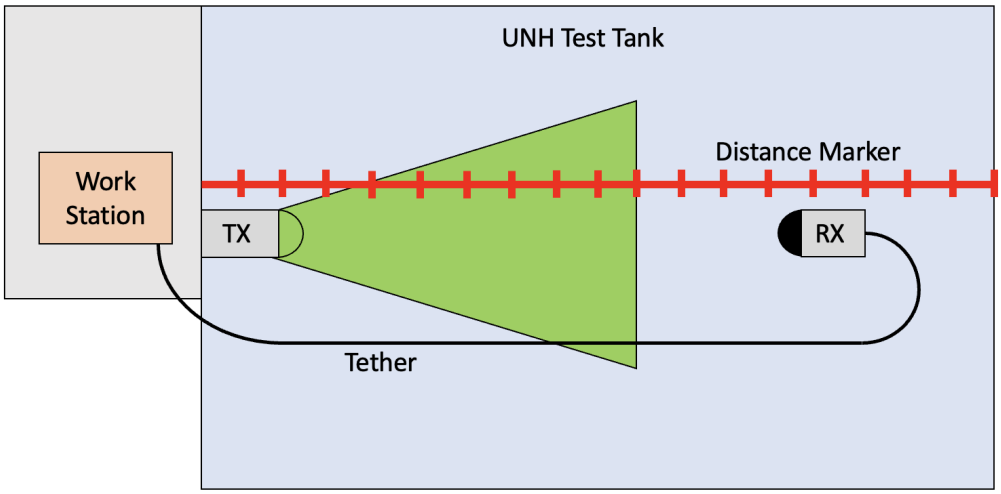

Figure 4.3: Underwater system test setup diagram

The receiver is then separated from the transmitter at 1m increments, pointing with direct line of sight with the transmitter. All received signals are recorded at the shore station. These steps are conducted for blue, green, and violet LEDs selected in Chapter 2. Figures 4.5 through 4.8 below show plots with the result summaries for each color.

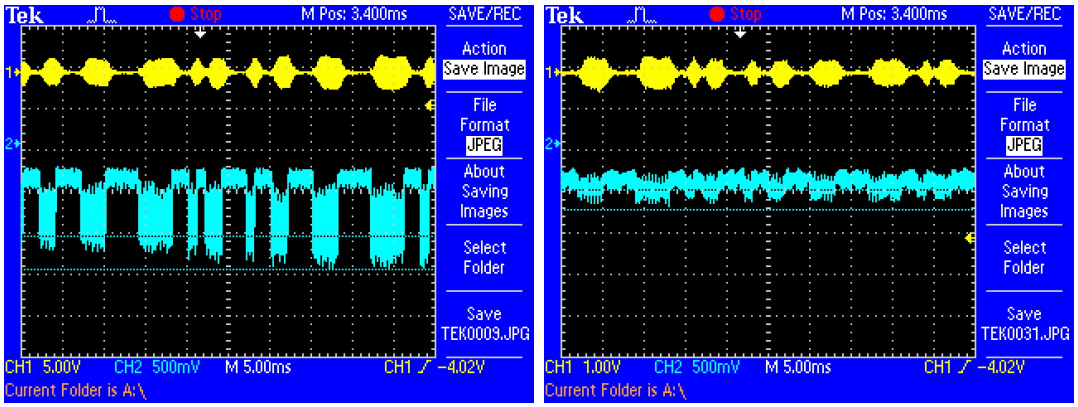

Figure 4.4: Blue (470nm) received signal at 10m (left) and 18m (right)

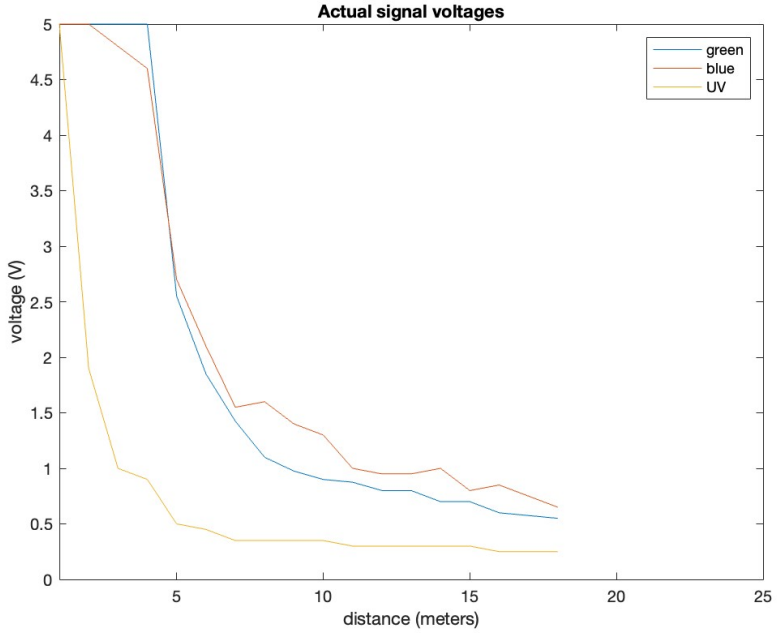

Figure 4.5: Actual TIA voltages

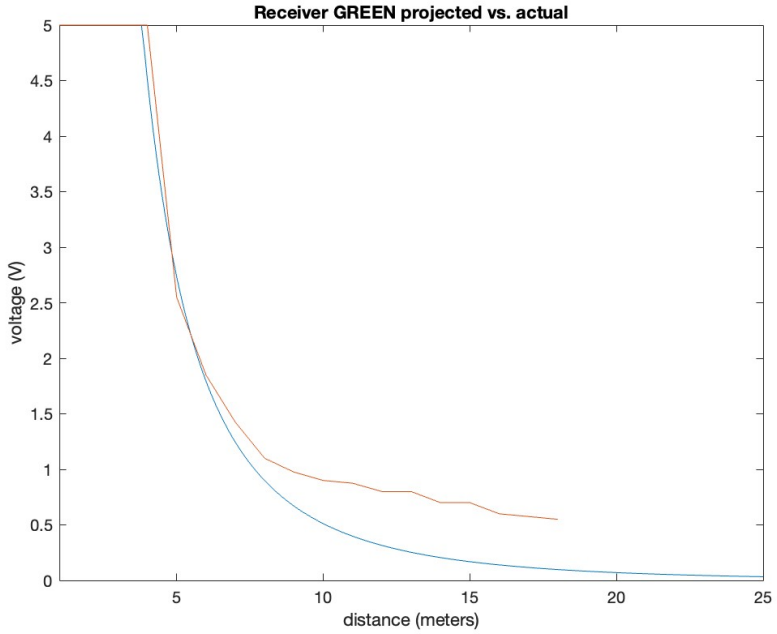

Figure 4.6: Green (520-525nm) actual vs. predicted

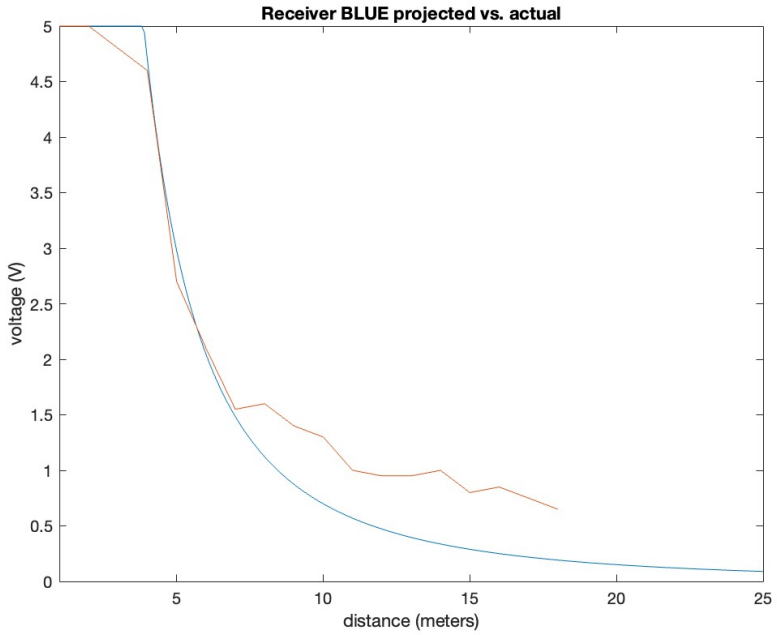

Figure 4.7: Blue (460-470nm) actual vs. predicted

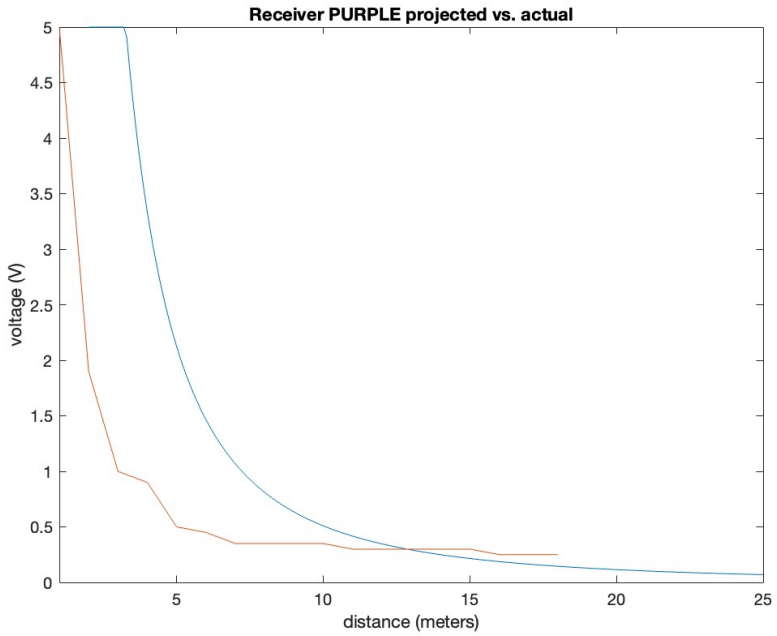

Figure 4.8: Violet (400nm) actual vs. predicted

There are two main phenomenons seen in the results:

- All colors are passing predicted values (blue and green at 7m and violet at 13m).

- Violet performance is significantly lower than that of predicted values, while blue and green performance roughly matches predicted values.

The first observation is determined to be caused by light's reflection from the water's surface, which becomes significant at approximately the 7-meter mark. Figure 4.9 shows a diagram utilized to examine this observation.

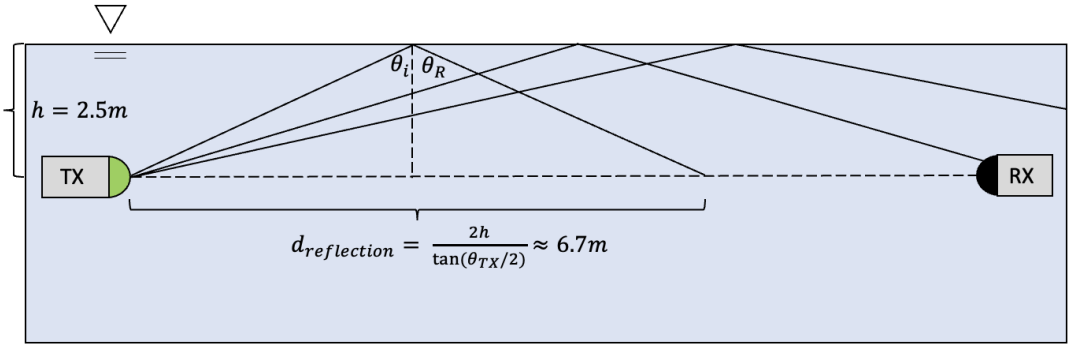

Figure 4.9: Light reflection diagram

The minimum reflection distance is calculated by utilizing instrument depth (2.5m), transmitter's dispersion angle (73.74°) and Snell's law, which yields the fact that $\theta_i = \theta_R$ [44]. The following equation is utilized:

$$d_{reflection} = \frac{2h}{tan(\theta_{TX} \div 2)} \approx 6.7m \tag{4.1}$$

$d_{reflection}$ represents minimum distance from the transmitter affected by the light's reflection from the surface, h represents the instrument's depth, and θ_{TX} represents transmitter's dispersion angle. Based on calculations, reflection starts affecting receiver's performance just prior to the 7m mark, which matches measured observations (Figures 4.5-4.8). Figure 4.10 shows an image of transmitted light reflected from the tank's water surface.

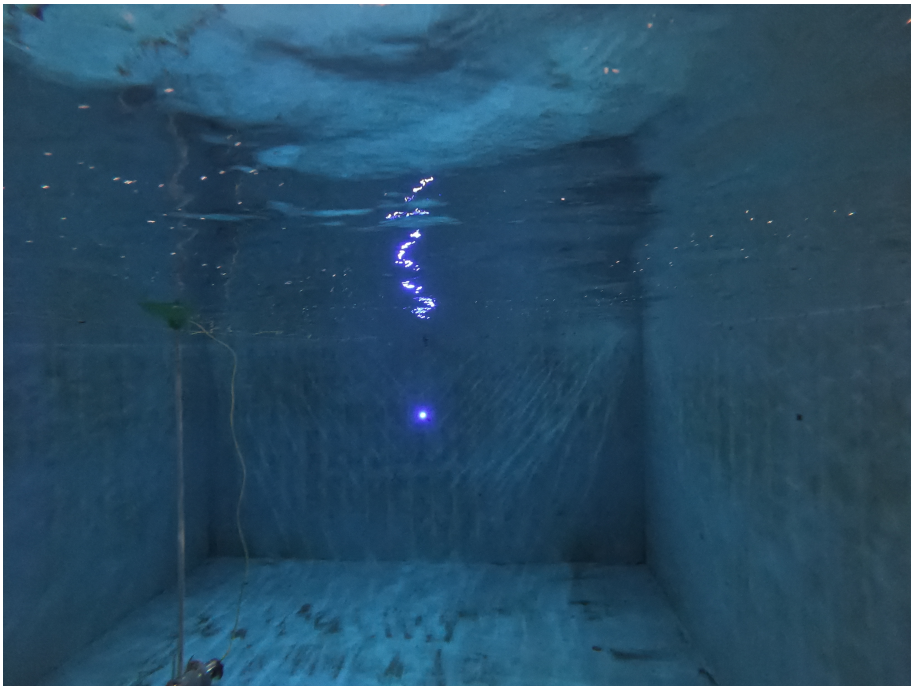

Figure 4.10: Light reflection path from the water surface

Due to the limited tank size and a fairly strong light source, avoiding reflection during testing is not possible. It is, therefore, simply excluded from the system's performance calculations in the future chapters.

The second observation of poor UV LED performance is also analyzed. This phenomenon is described by poor LED efficiency common among the UV LEDs. According to Professor Iftikhar Ahmad of University of South Carolina, current UV LEDs offer efficiencies of about 4-10% (compared to 80-90% for typical non-UV LEDs) due to high tendencies for absorption and internal reflection within materials utilized [45]. Typical UV-LED spectra ranges between 210-360nm [46]. The LED utilized in this experiment (400nm) is somewhat close to this range. As a result, UV LED's efficiency η is adjusted to match observed values and results in approximately 15% efficiency, which is much lower than the value of 90% utilized to calculate predicted values. Figure 4.11 shows the adjusted plot.

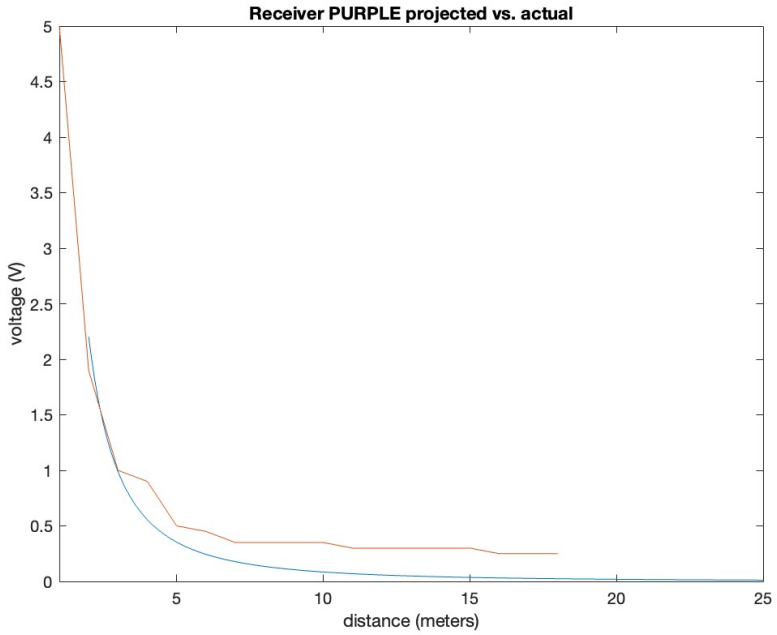

Figure 4.11: Violet LED (400nm) actual propagation compared to prediction adjusted for efficiency of 15%

Due to poor efficiency and limited power available onboard UUVs, violet LED transmission is not recommended and is removed from further considerations. If efficiencies are improved by manufacturers in the future, this option can be reassessed. Blue-Green spectra is recommended for optical communication depending on the water type (discussed in Chapter 1). Blue wavelength (460-470nm) is utilized for the remainder of this research due to clear water properties of the UNH Engineering Tank.

As the next step of system's analysis, signal strength and Signal-to-Noise Ratio (SNR) of the analog stage (Figure 3.19) are measured and analyzed. All resistance and capacitance values are reverted to those calculated in Chapter 3. That's $R_F = 10k\Omega, C_F = 10pF, R_2 = 1k\Omega$ and $R_3 = 10k\Omega$. The experiment is setup in the same manner as that previously discussed (Figure 4.3), and the signal strength is recorded as the receiver is moved away from the transmitter. Additionally, signal strength values are obtained for various receiver divergence angle values with gradations of rotation away from the light source. Projected

signal values are calculated with the following equation:

$$V_{out} = I_D R_F \left(\frac{-R_3}{R_2}\right) K_{filter} \left(\frac{-R_5}{R_4}\right) \tag{4.2}$$

Where I_D represents the photocurrent calculated in Equation (3.14), R_F represents the feedback resistor, K_{filter} represents the bandpass filter gain (1.122 per design specifications [38]) and R_4 and R_5 represent the respective resistor values of the post-filter op-amp with a gain of 10 ($R_4 = 1k\Omega, R_5 = 10k\Omega$). A plot containing captured signal values and a projected trend calculated above is shown in Figure 4.12, and two signal screen capture examples are shown in the Figure 4.13. A significant gap is present between observed and predicted SNR values, with observed signal values being greater than predicted.

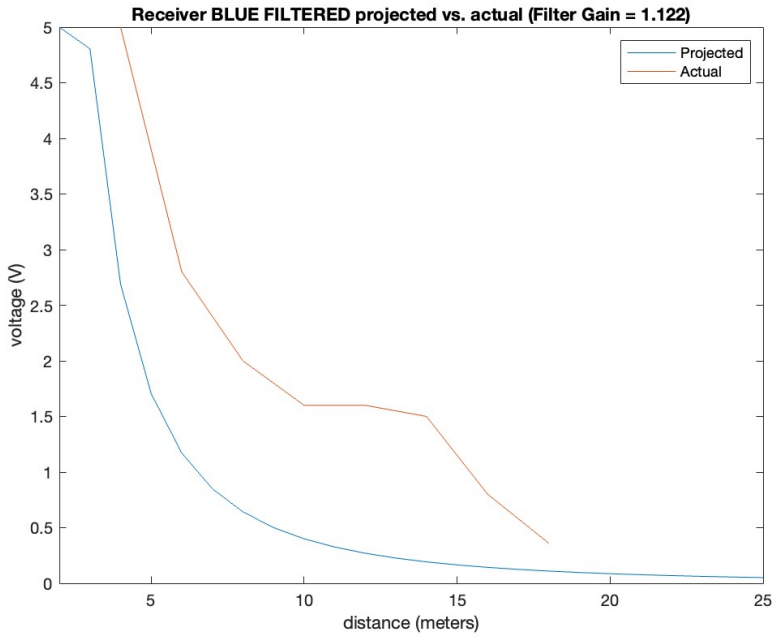

Figure 4.12: Projected (blue) vs. collected (yellow) signal values of the filtered analog stage

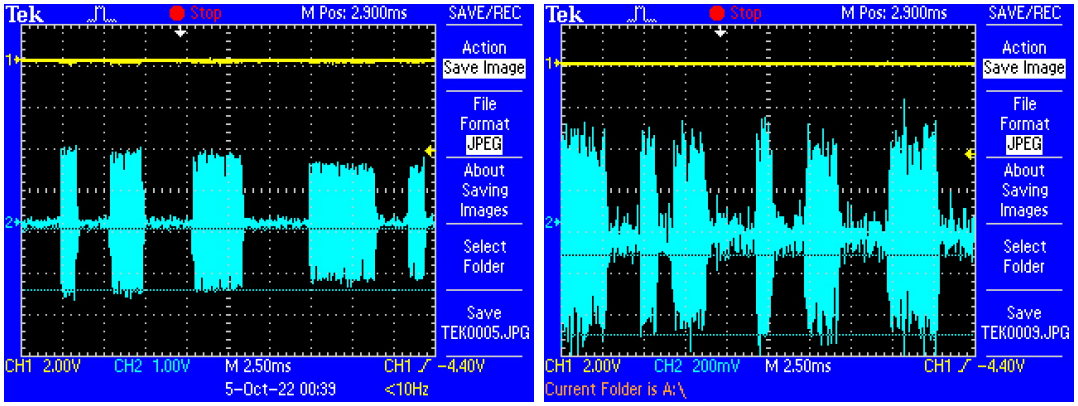

Figure 4.13: Blue (470nm) filtered signal strength at 10m (left) and 18m (right)

A significant gap between projected and actual values is determined to be caused by the filter gain of $K = 1.122$. All other values are known and verified. Filter gain is, therefore, adjusted to a new value of 2.6 to match collected data points (shown in Figure 4.14).

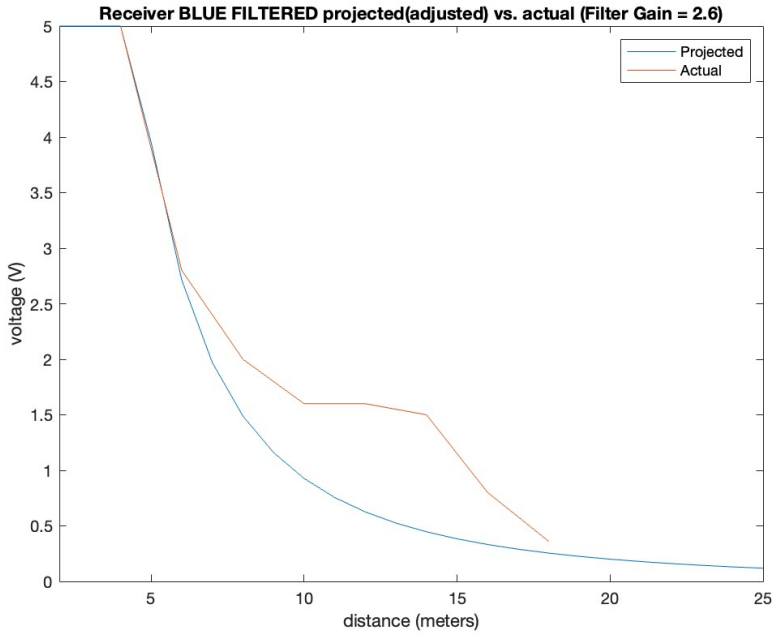

Figure 4.14: Projected (filter gain K adjusted to 2.6) vs. collected signal values of the filtered analog stage

A signal-to-noise ratio (SNR) is calculated and plotted based on the measured noise floor value of 120mV. SNR plot is shown in Figure 4.15. At this point of design, an SNR value

of 2 is determined to be the smallest discernible signal, which yields a maximum detectable range of just over 18m in clear water. Actual minimum (i.e., readable) SNR values will be tested and presented in Chapter 5.

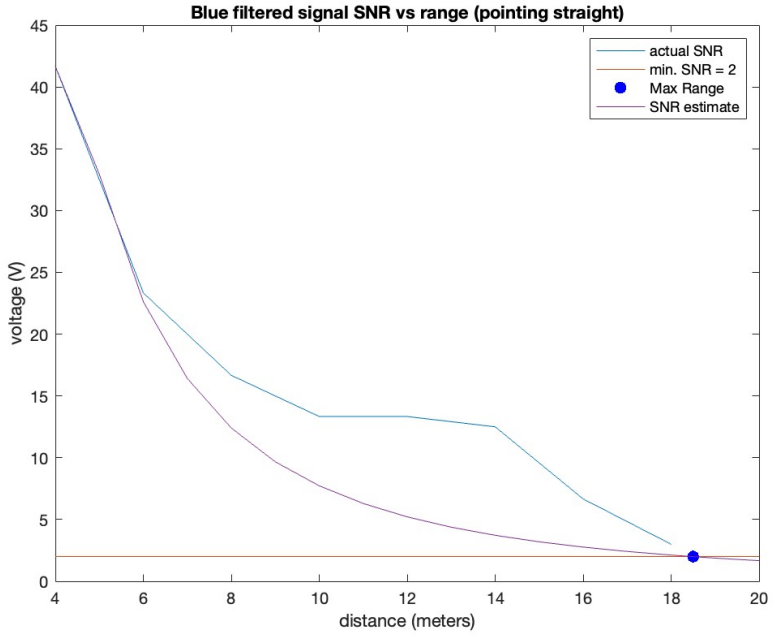

Figure 4.15: Signal-To-Noise Ratio

In addition to signal deterioration with increasing distances away from source, signal attenuation vs. divergence angle is measured. Signal values are recorded as the receiver is turned away from the transmitter. Figure 4.16 shows the plot of captured values and a "trend line" function fitted to match collected data points such that

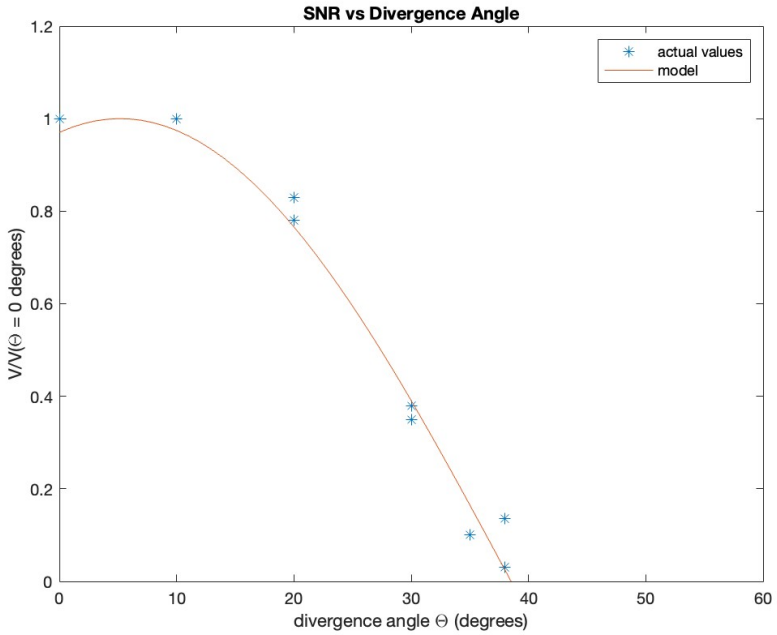

Figure 4.16: Signal vs. Divergence Angle θ

$$\frac{V}{V_{\theta=0}} \approx cos(2.7\theta - 14) \tag{4.3}$$

Based on the Eq.(4.3) (as well as experimental results), receiver signals become unreadable at divergence angles greater than 39 degrees regardless of the distance from the transmitter. Based on signal attenuation due to increasing range and/or angle, a performance model is constructed and is shown in Figure 4.17. It can be seen that this design is capable of receiving readable signals (assuming SNR=2 is readable) at distances of over 18 meters with direct line of sight, and distances of 15 meters with divergence angles of less than 30 degrees from the source. If greater distances are required, a more powerful transmitter LED can be utilized and modeled with the steps discussed in Chapters 2-4.

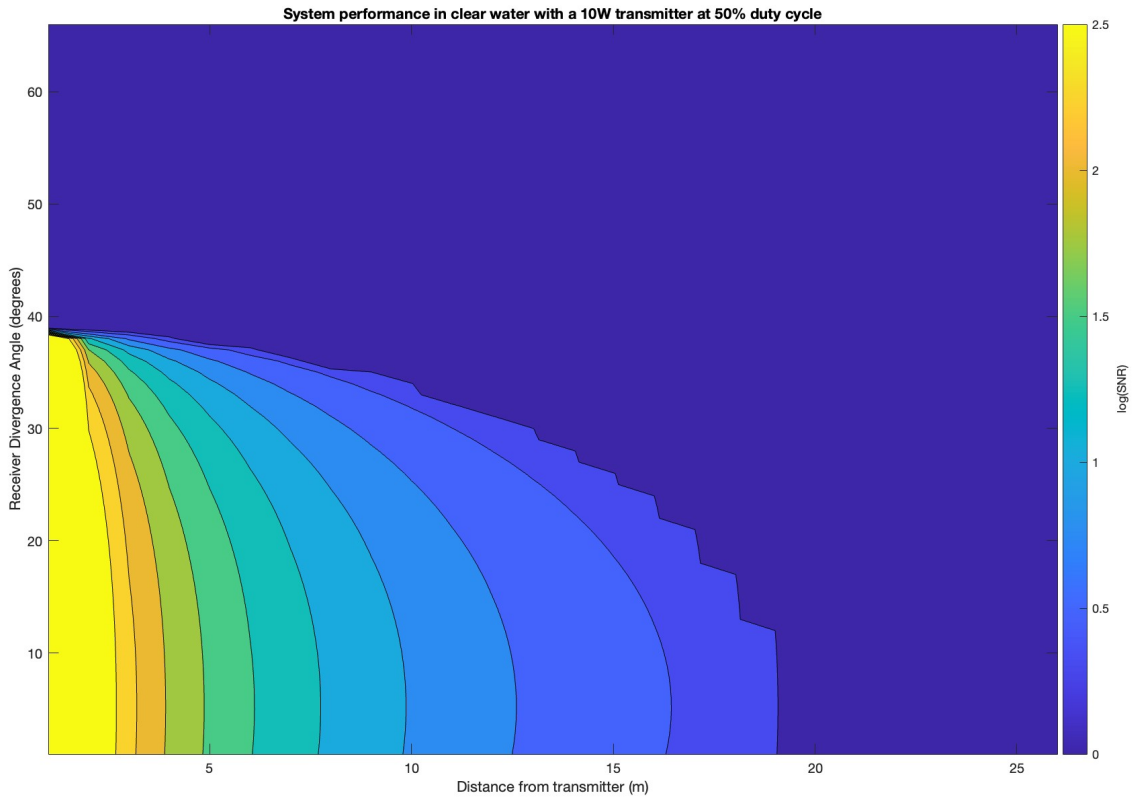

Figure 4.17: Optic communication system's calculated performance in the UNH engineering tank (clear water)

CHAPTER 5

Digital Signal Processing

5.1 Reading And Interpreting Incoming Messages

Once filtered and digitized signal enters the processing board's I/O pin, the following steps and procedures take place to recognize the message:

- Interrupts are set up for the I/O pin. This enables the electrical circuit to detect incoming signal and move into its Interrupt Service Routine (ISR) [25] to start the signal processing routine. High-To-Low interrupts (i.e., signal drops) trigger a different ISR function compared to that of Low-To-High interrupts (i.e., signal rise).
- Bit length is determined based on the system's transmission speed. For example, for a 5kbps transmission rate, a length of one bit is 200us.
- A Delta value is pre-determined to indicate to the system where in the message structure 1-bits are interpreted.
- Timers are incorporated to capture the duration of "1" (one_timer) and "0" (zero_timer)

As the signal enters the electrical configuration, it pulses with a frequency f_C during a binary "1" for the duration of a length of one bit (bit length). During a binary "0", the signal is low for the bit length duration. Figure 5.1 shows a visual diagram of the bit interpretation process.

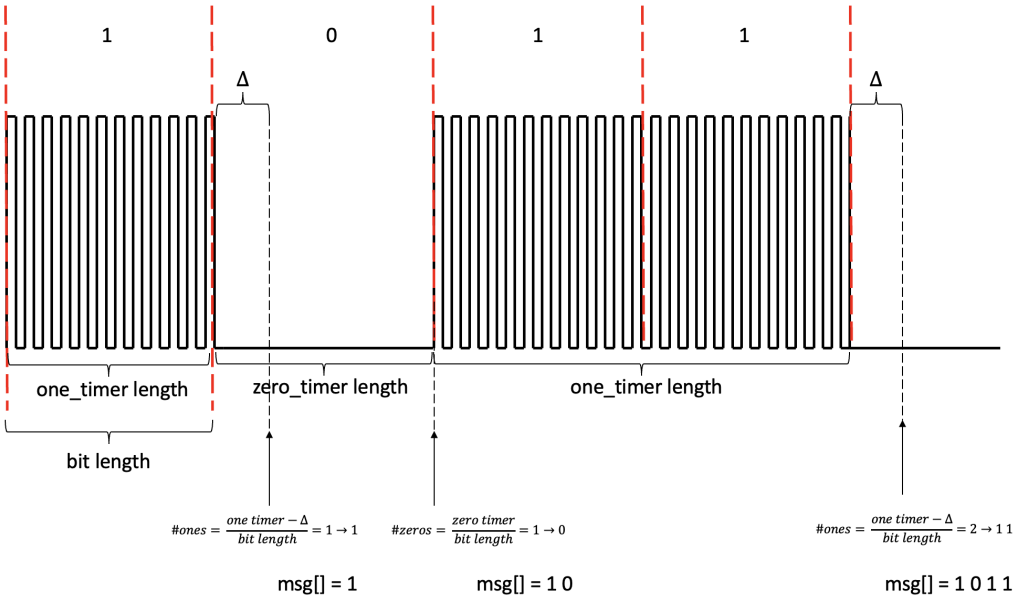

Figure 5.1: Signal Interpretation Diagram

Once the signal is detected (during a Low-To-High interrupt) a one_timer starts recording the length of "ones" being transmitted. Once the signal returns to a binary "zero" (determined by the Delta threshold as shown in the Figure 5.1), the amount of transmitted "ones" is calculated and added to the message queue (an array of binary values). The following equation calculates the amount of "ones":

$$N_1 = \frac{one\ timer - \Delta}{bit\ length} \tag{5.1}$$

In a similar fashion, when the signal reaches another binary "one" (Low-To-High interrupt), the amount of transmitted zeros is calculated and added to the message queue with

$$N_0 = \frac{zero\ timer}{bit\ length} \tag{5.2}$$

Figure 5.2 shows a detailed flow chart of this algorithm, and Appendix A1 provides the pseudo code implemented in this research. In addition to the items previously discussed,

this algorithm continuously times activity on the receiver's I/O pin and triggers a message timeout if this timer passes a certain threshold (determined by the user). If timeout is detected, all flags, timers, interrupts and values are reset to those equivalent of a "standby and listen" mode.

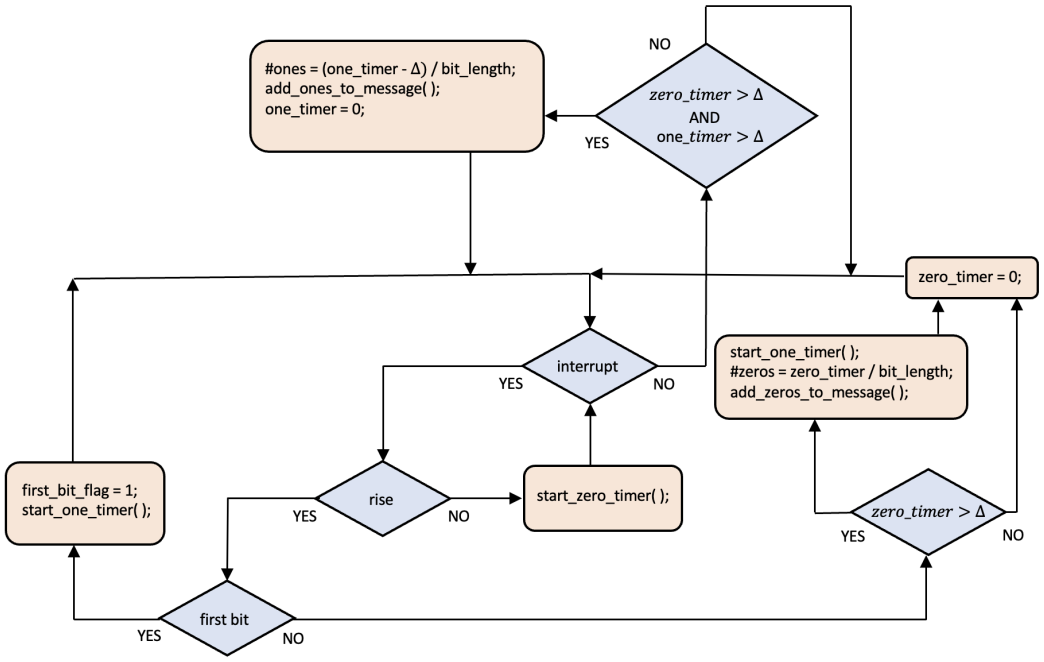

Figure 5.2: Signal interpretation flow chart

A clear disadvantage in using this software structure is that any random noise values during binary zeros may cause premature readings and result in either extra or missing bits in the detected message. This phenomenon causes a shift in the message and prevents the circuit configuration from enabling successful message recognition. In order to minimize this error, a short packet structure is selected. Figure 5.3 shows the packet structure chosen for this work. The packet structure consists of:

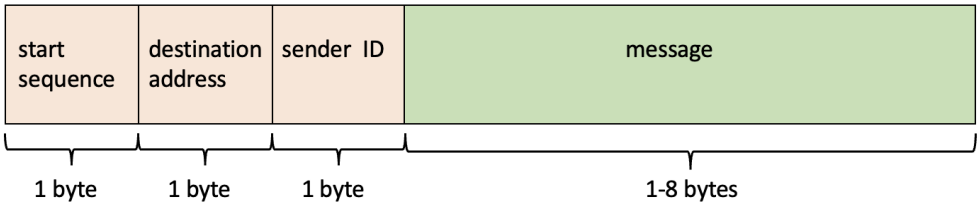

Figure 5.3: Message packet structure

- Start sequence - enables the electrical board to distinguish an actual message from noise. In this work, 0010 1100 (0x2C) is selected as the start sequence, and the board begins to interpret the remainder of the packet once starting sequence is spotted.
- Destination address - an address of the intended recipient. This portion is intended to enable senders to transmit traffic to specific nodes in a multi-UUV network.
- Sender ID - an address of a node sending the message. As with the destination address, this portion of the packet enables multi-UUV communication protocol.
- Message - a body of a message containing short messages/commands (e.g., control/-position commands).

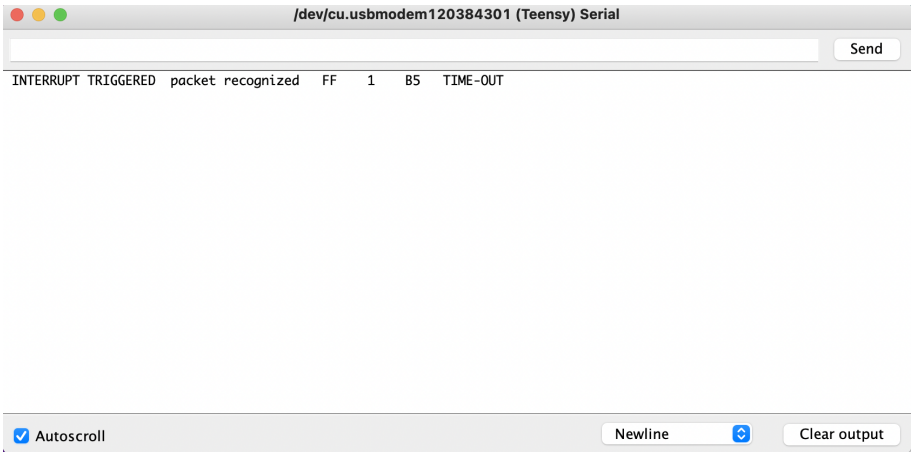

Figure 5.4: Example message captured during system testing

Figure 5.4 above shows a small message captured during system's testing. Instead of outputting 0x2C (start packet), the electrical board prints "packet recognized" statement to

alert the user that the message is successfully identified as valid. Following the statement, the message contains a destination address of 0xFF (all nodes), a sender's ID of 0x01 (node 1), and a message body of 0xB5 (random HEX value chosen).

5.2 System Performance Experiment

To analyze the system's overall performance and limitations caused by the digital processing error, an experiment is set up and bit-error-rate is measured for various divergence angles and SNR values. To start with, the receiver is placed such that it is pointing directly at the transmitter (i.e., no divergence angle). The transmitter is programmed to transmit a randomly generated 10-byte message (excluding the start sequence), which is recorded via a serial terminal once captured and processed by the receiver. This process is conducted ten times per angle for the following divergence angle values: 0° 10° 20° 30° 35° *and* 38°. Figure 5.5 shows the diagram of this experiment's setup.

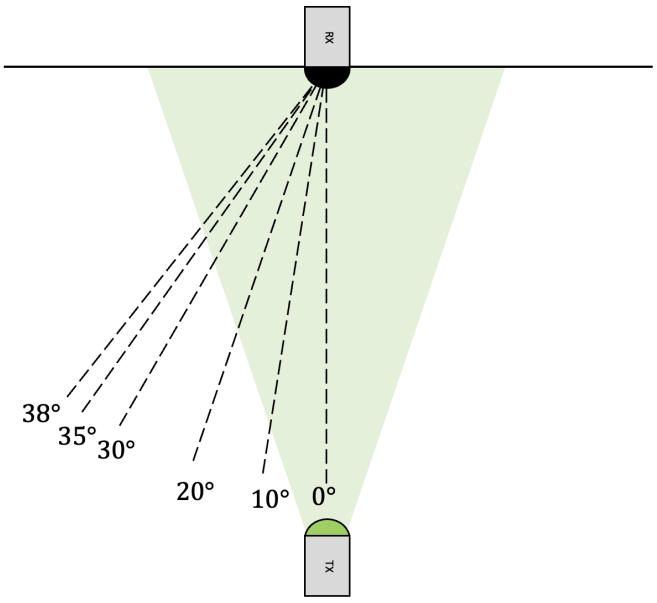

Figure 5.5: Bit-Error-Rate experiment setup

In addition to the angle and signal values, SNR values are also recorded. The following binary sequence is randomly generated and programmed into the transmitter:

7B 4E 85 5C 5C 5C 50 ED 00 C4

Two separate transmission modes are recorded for this experiment: continuous transmission (constant flashing) and a single message (flashing every 2 seconds). Figures 5.6 through 5.9 show the resulting bit error rates.

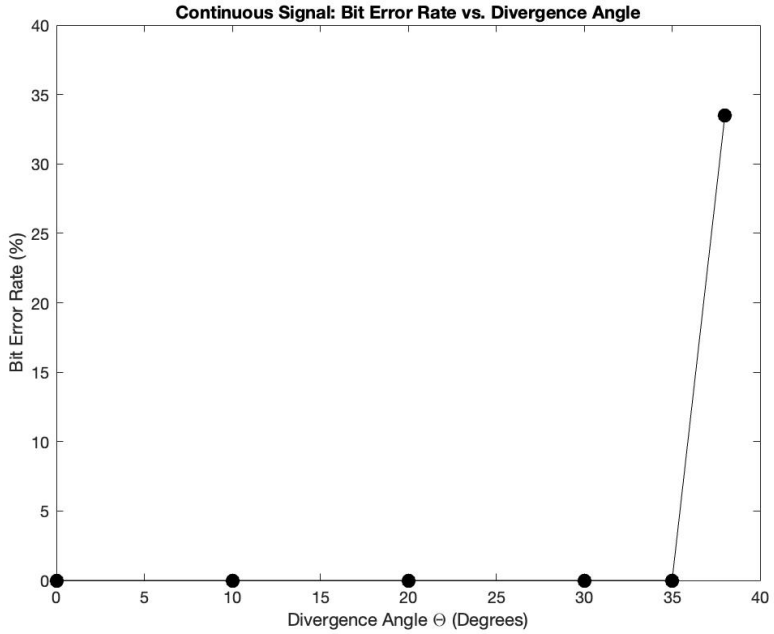

Figure 5.6: Bit-Error-Rate vs. Divergence Angle during continuous transmission

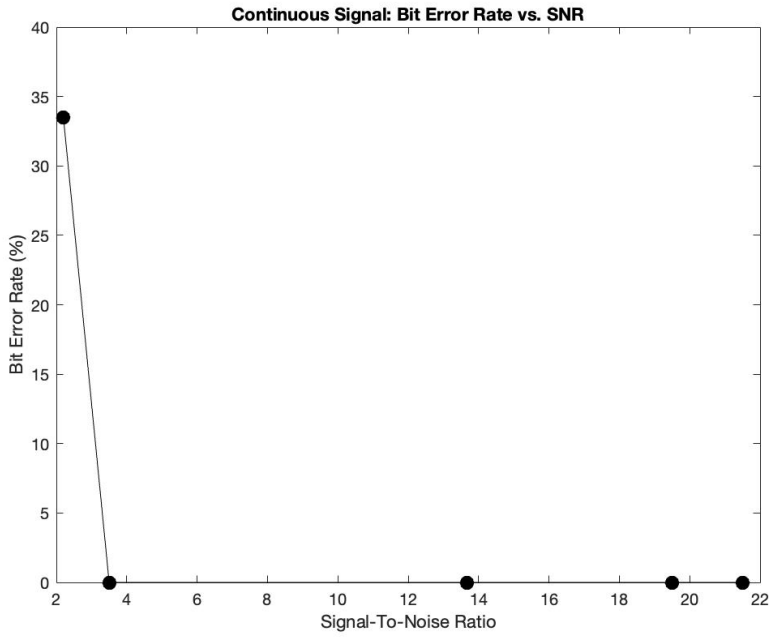

Figure 5.7: Bit-Error-Rate vs. SNR during continuous transmission

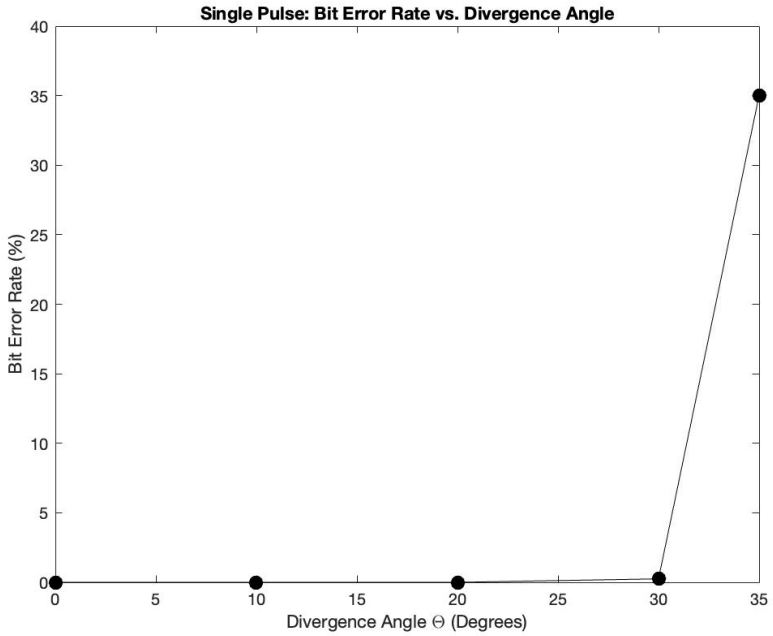

Figure 5.8: Bit-Error-Rate vs. Divergence Angle during single-pulse transmission

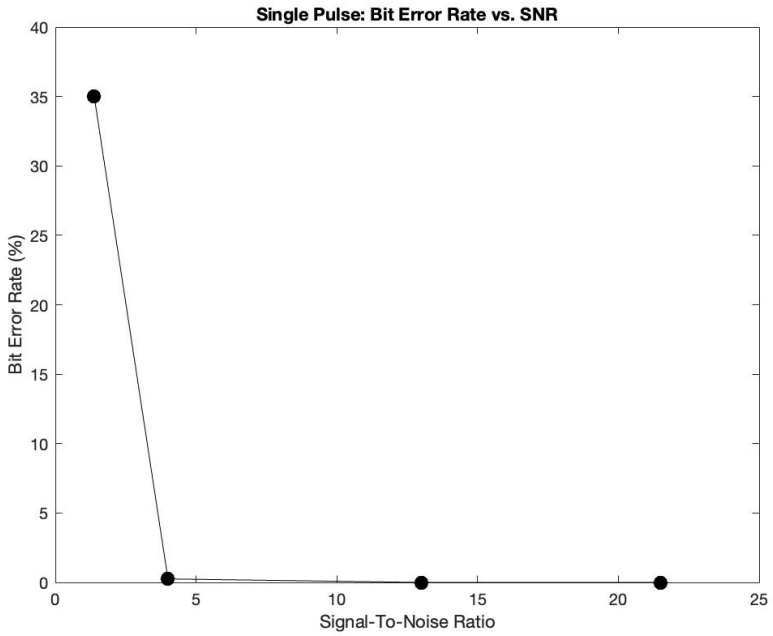

Figure 5.9: Bit-Error-Rate vs. SNR during single-pulse transmission

To summarize the results, the system's performance is acceptable and transmission is appropriately accurate for SNR values of greater than 4. Single-pulse transmission shows

weaker SNR values for the same source distances (and, therefore, lower divergence angle limits). In addition to the SNR, it is determined that the system in its current configuration can not process incoming data at divergence angles of greater than 35° regardless of transmission range. Based on these experimental findings, a new performance plot (adjusted for SNR and angle) is shown in Figure 5.10. In short, the current system configuration can accurately transmit, receive, digitize and interpret data packets at ranges of just under 15 meters (pointing directly at its target receiver) and divergence angles of up to 35° (but with lower transmission ranges).

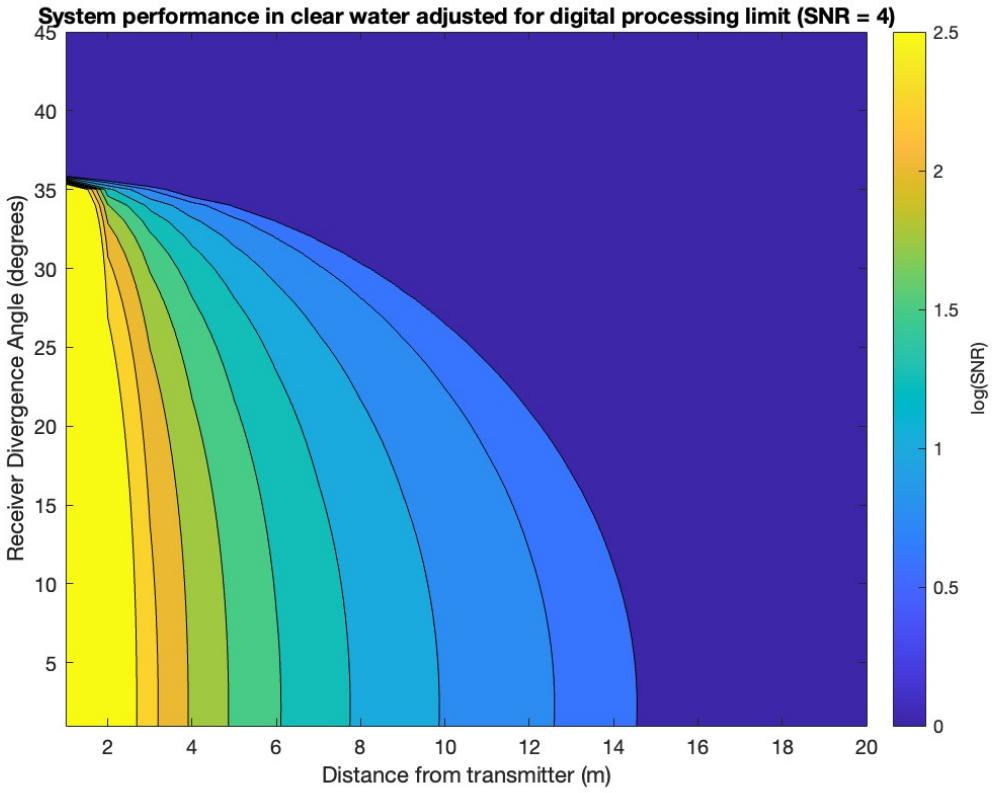

Figure 5.10: calculated system performance adjusted to a minimum value of SNR=4

CHAPTER 6

Multi-UUV Communication

6.1 Two-Node Communication

Based on the research and experimental data achieved in previous chapters, this experiment's two-way communication is achieved via two different transmitter LED wavelengths and corresponding carrier frequencies. First, communication nodes are configured as shown in Figure 6.1. The transmitter and receiver boards are connected to each other via serial communication, and receiver board's I/O pins are connected to small LEDs. For two-way communication, Node 1 transmits via blue LED and Node 2 via a green LED.

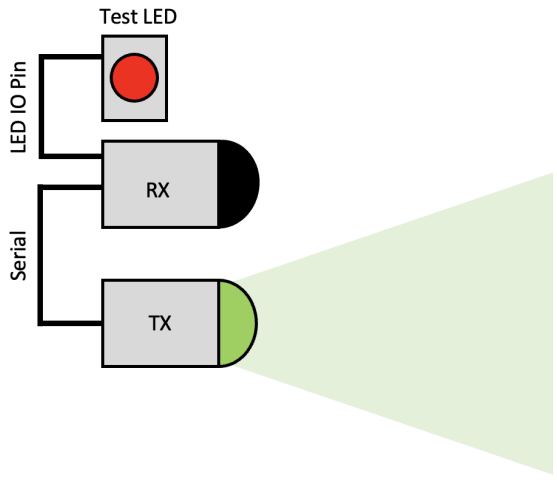

Figure 6.1: Optical Communication Node Setup

Each node's optic filters are set up to receive each wavelength accordingly. In addition to different LED spectra, two nodes utilize different carrier frequencies: Node 1 transmits at

10kHz, while Node 2 transmits at 100kHz. Each receiver's band pass filter frequencies are adjusted accordingly. 1kbps bit rate is utilized for this experiment to enable data processing for a 10kHz receiver. The bit rate-to-f_C ratio is less than 1/20 but message processing is still possible, albeit not optimal. Figure 6.2 shows the two-node setup.

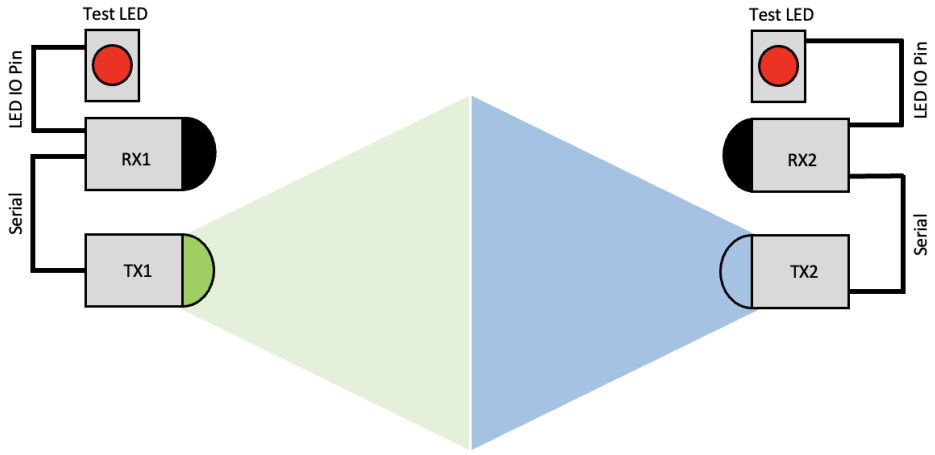

Figure 6.2: Two-Node Communication

The following sequence is implemented to test this two-node communication configuration:

- Node 1 (flash LED) to Node 2. If the message is received, Node 2 flashes a test LED.
- Node 2 (flash LED) to Node 1. If the message is received, Node 1 flashes a test LED.
- Repeat sequence

During this experiment it is found that both nodes successfully interpret incoming messages with simultaneous transmission (i.e., when Node 1 and Node 2 flash messages at the same time). Both nodes successfully and reliably flash their respective test LEDs as a sign of confirmation.

6.2 Higher-Node Communication

Even though it is shown that communicating with different carrier frequencies and different light wavelengths is an effective method based on the aforementioned experiments, this method is not feasible for a network of three or more nodes (UUVs) in the configuration used in this research mainly because of the high number of sensors and instrumentation required. Each f_C and light wavelength requires its own dedicated transmitter-receiver pair. Therefore, a multiplexing approach is taken to resolve this requirement. Multiplexing method is common in today's telecommunication systems and involves combining two or more information channels into a single transmission medium [47]. Specifically, a time division multiplexing (TDM) scheme is utilized, which involves merging multiple data streams into a single communication channel by separating the time window into multiple segments [47]. In this case, each UUV is given a certain time window to transmit information, as shown in Figure 6.3 for a 3-UUV communication network configuration

	Time Window 1	Time Window 2	Time Window 3	...
NODE 1	X			
NODE 2		X		
NODE 3			X	
...				

Figure 6.3: Multi-Node Time Division Multiplexing

All UUVs use the same carrier frequency and light wavelength, and, instead, subdivide a single communication channel into multiple time segments. A 300kHz carrier frequency and 5kbps bit rate are utilized in this research. First, transmission length of one packet (Packet Length) is calculated for a packet size of 11 bytes and transmission speed of 5kbps:

$$PL = \frac{packet\ length}{bit\ rate} = \frac{11\ bytes \times 8\ bits/byte}{5kbps} = 17.6ms \tag{6.1}$$

Where PL represents packet length. For a 17.6ms packet, a 20ms Window Length (WL) is assumed. A TDM timing diagram is shown in Figure 6.4. Each UUV (node) is given a

20ms window to transmit data, where packet transmission must start between the beginning of this window and $\Delta t = WL - PL = 2.4ms$ after the window start to avoid overlap with the next node's transmission window. The combined channel bit rate is calculated with the following equation:

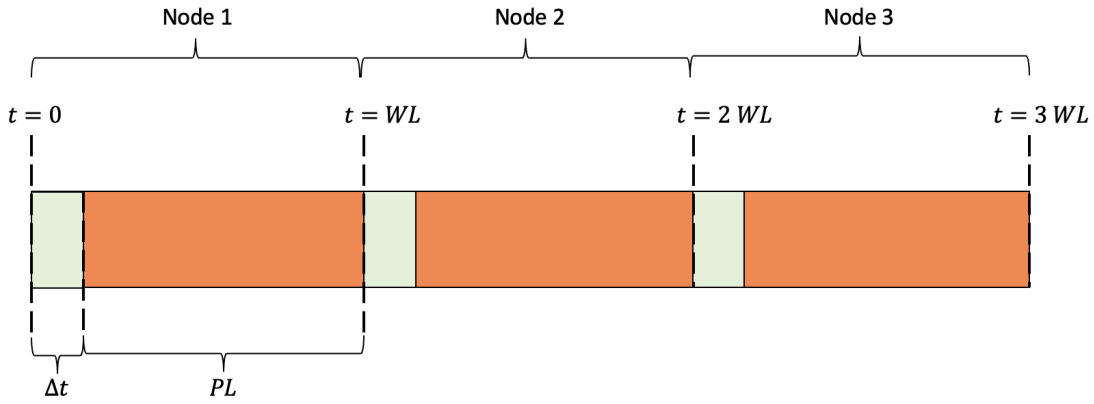

Figure 6.4: TDM channel structure

$$Channel\ Bit\ Rate = \frac{Packet\ Size}{N_{Nodes} \cdot WL} = \frac{88\ bits}{3\ nodes \times 20ms} = 1.466kbps \tag{6.2}$$

where N_{Nodes} represents number of nodes (i.e., UUVs) on the network, and WL represents the length of time window of each node.

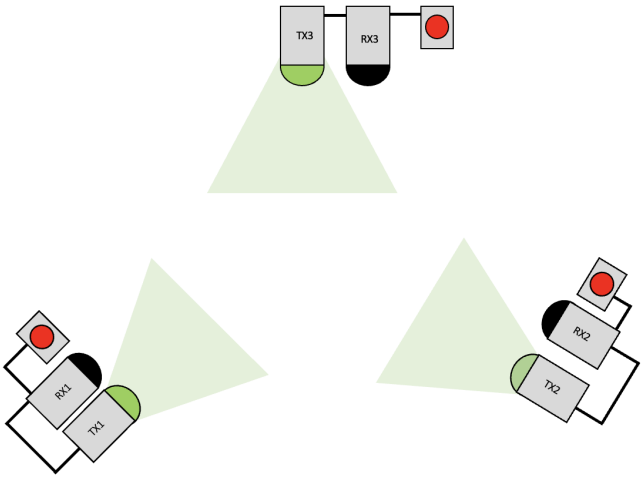

Figure 6.5: Three-Node Experimental Setup

To test this setup, three nodes are configured as shown in Figure 6.5. The nodes are placed in a static configuration at the angles sufficient to support sensor's divergence angle limits (discussed in Chapters 4 and 5). The following sequence is programmed into the network:

- All nodes await a command to initiate timers and commence communication.
- Node 1 transmits "start the timers and initiate communication" packet. (All nodes start timers simultaneously, and each node tracks its respective communication window as per Figure 6.4).
- Simultaneous communication between UUVs, where the test LED of each node has a 100ms timer associated with its LED, which turns off the LED unless constant "turn on LED" commands are received.
- Node 1 (flash LED) to Node 2. If the message is received, Node 2 flashes a test LED.
- Node 2 (flash LED) to Node 3. If the message is received, Node 3 flashes a test LED.

- Node 3 (flash LED) to Node 1. If the message is received, Node 1 flashes a test LED.
- Repeat sequence

Testing in this research is successfully completed with all test LEDs turning on (showing successful message reception in TDM sequence). One key note to discuss is the clock drift, where each Node's clock eventually drifts out of sync for reasons as aging and environmental factors and others [48]. To prevent the overlapping of communication windows between nodes, clocks must be periodically reset. For this study, a 1-minute interval is chosen as a time increment from which to reset all clocks. A detailed analysis of clock errors is not conducted in this experiment.

CHAPTER 7

Conclusion and Future Work

7.1 Future Work And Other Applications

Although all system components are successfully tested and yielded acceptable experimental results, some work still remains prior to successful integration into the UUV formation. First, a complete system must have a way to estimate maximum communication ranges in various water types. As discussed in Chapter 2, estimating light's attenuation coefficient K_d can be challenging, and variation between different water types can be significant (e.g., clear water compared to a turbid coastal harbor). The U.S. Environmental Protection Agency (EPA) offers a solution to this problem by implementing a nephelometry method. Turbidity can be determined by comparing the sample's scattered light intensity under defined conditions to the light intensity scattered by a standard reference suspension [49]. In other words, a photodiode detector can be centered at 90° to the incident light path (as shown on the left in Figure 7.1), which would detect light levels reflected from suspended particles (as shown on the right in Figure 7.1).

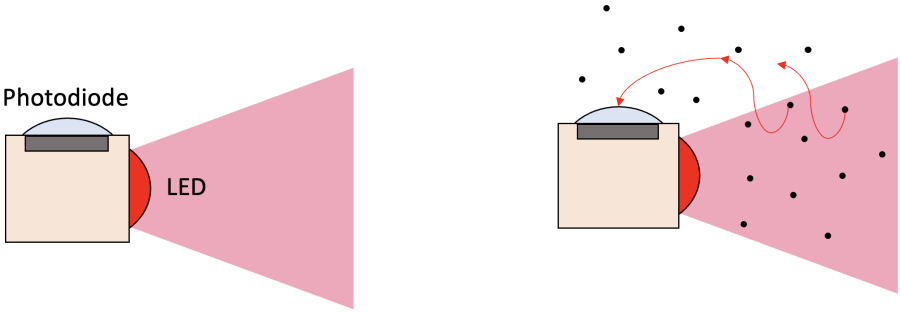

Figure 7.1: Nepholometry setup (left) and light reflection from suspended particles (right)

Light reflections in clear water are expected to be significantly less than those of turbid waters due to the amounts of suspended particles present. Photocurrent generated by the reflected light can be converted into a voltage and then digitized to be used for K_d calculations. These calculations would then yield communication range approximations. This data can then be used to adjust UUV formation ranges.

In addition to K_d approximation, the proposed configuration's analog-to-digital stage limits the system's overall performance. Specifically, the timing sequence is prone to error in the presence of noise during binary "0" transmission. As discussed in Chapter 5, a noise spike could inadvertently insert a character and shift the entire message. (For example, "0101" can mistakenly turn into "00101.") In other words, one bit error can distort the entire message. To improve Bit Error Rate (BER) each bit should be timed once in its center instead of utilizing timers. Figure 7.2 shows the process diagram.

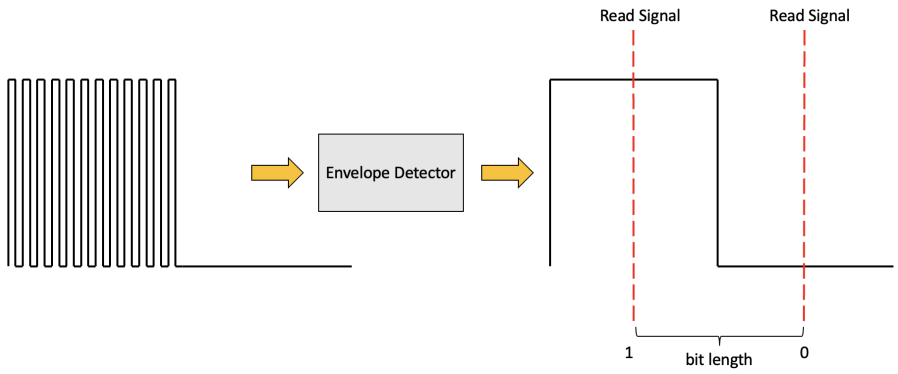

Figure 7.2: A more efficient timing method of a digital signal to improve BER

In this case, a single bit error does not affect the remainder of the message being processed. An envelope detector shown in the Figure 7.2 is already in place (created by the no-feedback ap-amp configuration discussed in Chapter 3 and shown in Figure 3.23). For future work, a digital signal processing scheme can be adjusted to match the timing sequence shown in Figure 7.2. This improvement could result in enhanced system performance and the ability to send larger data packets for longer communication ranges.

To successfully control a UUV formation, each vehicle must have a 360° reception view. A single PS100-6b photodiode sensor tested in this research is limited to a 70° divergence angle. Therefore, a photodiode array could provide a fully functioning 3-D system. In a two-dimensional setting, this can be achieved by placing sensors at 60-degree intervals as shown in Figure 7.3. Here, a60° divergence angle is chosen (instead of 70°) to accommodate a 10° overlap.

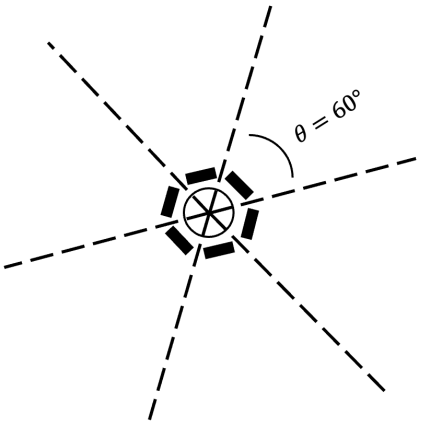

Figure 7.3: Concept for a 2-D array for enabling 360-degree reception

All photodiodes within the array can be connected in parallel as shown in Figure 7.4. Additional circuit analysis is required due to high C_D-capacitance values of each photodiode. A 360-degree 3-D view can be achieved in the same manner with additional photodiodes and calculations.

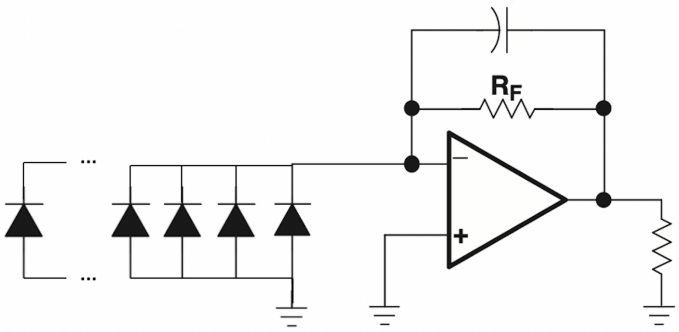

Figure 7.4: Photodiode array circuit

7.2 Difficulties And Advice To Future Students

Even though there was no "easy" part of this research, some areas presented more challenges than others and required creative solutions. In general, this work relies heavily on analog electronics and circuit analysis. In addition to taking ECE coursework and getting familiar with analog electronics, I strongly encourage students interested in this work to refer to

and get familiar with The Art Of Electronics by Paul Horowitz and Winfield Hill [50]. This reference contains tools to many creative solutions utilized throughout this research. Another advice is to divide projects into small increments and test as often as possible. Troubleshooting small components (e.g. TIA, BPF, A-to-D...etc) was significantly easier than attempting to tackle the entire system.

7.3 Conclusion

In short, a cost-efficient, short distance optical communication system capable of supporting formation control of multiple UUVs is designed and tested. Underwater light propagation is studied and tested, yielding a method to model and predict transmitter and receiver performance at various ranges and divergence angles. Receiver circuit is designed and implemented, enabling signal filtering and processing. And finally, a multi-node TDM protocol is created and tested, allowing for multi-UUV communication via the same optical wavelength, λ, and carrier frequency, f_C. An experimental proof-of-concept of all subsystems is provided, which shows the proposed optical communication system as viable for future full integration.

LIST OF REFERENCES

[1] Dr. May-Win Thein. Oe817 marine robotics. In-Person class at University of New Hampshire, 2022.

[2] NOAA Ocean Exploration. Technical diving. `https://oceanexplorer.noaa.gov/technology/technical/technical.html`, 2022. Accessed: 2022-11-08.

[3] Helge Renkewitz Kay Strama, Daniel Weber. Evaluation of wifi data transmission algorithms for short distance underwater communication. *OCEANS 2021: San Diego-Porto*, 2021.

[4] Technoligy Editor. Underwater communications for uuv, auv, rov. `https://www.unmannedsystemstechnology.com/expo/underwater-communications/`, 2022. Accessed: 2022-11-09.

[5] HYDROMEA. Exray the world's first wireless rov. `https://www.hydromea.com/exray-wireless-underwater-drone`, 2022. Accessed: 2022-10-18.

[6] Dr. Thomas Weber. Oe865 underwater acoustics. In-Person class at University of New Hampshire, 2021.

[7] Jeffery DeArruda Joe Borden. Long range acoustic underwater communication with a compact auv. *OCEANS*, 2012.

[8] Akram Al-Hourani Henrique Matzenbacher Duarte and Richardt Wilkinson. Performance optimisation for underwater acoustic chirp communication. *2021 31st International Telecommunication Networks and Applications Conference (ITNAC)*, 2021.

[9] Shiraz Shahabudeen Mandar Chitre. Underwater acoustic communications and networking: Recent advances and future challenges. *Marine Technology Society Journal*, 2008.

[10] Woods Hole Oceanographic Institution. Whoi micromodem. `https://acomms.whoi.edu/micro-modem/`, 2018. Accessed: 2022-10-17.

[11] Hanumant Singh Jeffrey W. Kaeli. Illumination and attenuation correction techniques for underwater robotic optical imaging platforms. *Woods Hole Oceanographic Institution*, 2022.

[12] Fabio Leccese Giuseppe Schirripa Spagnolo, Lorenzo Cozzella. Underwater optical wireless communications: Overview. *MDPI Journal*, 2020.

[13] Andreas Birk Tomasz Łuczyński. Underwater image haze removal with an underwater-ready dark channel prior. *ResearchGate*, 2017.

[14] Chuying Yu Jiannan Shen, Jiongliang Wang. Single led-based 46-m underwater wireless optical communication enabled by a multi-pixel photon counter with digital output. *Elsevier*, 2019.

[15] HYDROMEA. Luma fast underwater wireless communication. https://www.hydromea.com/underwater-wireless-communication, 2022. Accessed: 2022-10-18.

[16] Edmund Optics. Fundamentals of lasers. https://www.edmundoptics.com/knowledge-center/application-notes/lasers/fundamentals-of-lasers/#diodes, 2022. Accessed: 2022-11-09.

[17] Heather Brundage. Designing a wireless underwater optical communication system. Master's thesis, Massachusetts Institute of Technology, Cambridge, MA, 2010.

[18] D Ulfah B Nababan and J P Panjaitan. Light propagation, coefficient attenuation, and the depth of one optical depth in different water types. *IOP Conference Series*, 2021.

[19] Amazon/Chanzon. Chanzon high power led chip 10w. https://www.amazon.com/Chanzon-Intensity-Emitter-Components-Lighting/dp/B01DBZK0ZA?th=1, 2022. Accessed: 2022-10-25.

[20] Edmund Optics. 50mm diameter x 44mm fl, pcx condenser lens. https://www.edmundoptics.com/p/50mm-diameter-x-44mm-fl-pcx-condenser-lens/5156/, 2022. Accessed: 2022-10-25.

[21] Penn State University Center of Nanoscale Science MRSEC. Light bulb efficiency. https://www.mrsec.psu.edu/content/light-bulb-efficiency, 2018. Accessed: 2022-10-25.

[22] Edward S. Fry Frank M. Sogandares. Absorption spectrum (340–640 nm) of pure water. photothermal measurements. *Applied Optics*, 1997.

[23] Wavelength Electronics. Photodiode basics: Selection operation. https://www.teamwavelength.com/photodiode-basics, 2020. Accessed: 2022-11-07.

[24] Winfield Hill Paul Horowitz. *The classic oscillator-timer chip: the 555*, pages 428–430. Cambridge University Press, New York, NY, 2021.

[25] PJRC. Teensy 4.0 development board. https://www.pjrc.com/store/teensy40.html, 2020. Accessed: 2022-11-07.

[26] Jerald Greame. *Photodiodes*, pages 1–20. McGraw-Hill, New York, NY, 1996.

[27] Hamamatsu. Si apds. https://www.hamamatsu.com/us/en/product/optical-sensors/apd/si-apd.html, 2022. Accessed: 2022-11-10.

[28] Edmund Optics. Hamamatsu avalanche photodiodes. https://www.edmundoptics.com/f/avalanche-photodiodes/13075/, 2022. Accessed: 2022-11-10.

[29] Wavelength Electronics. Photodiode basics. https://www.teamwavelength.com/photodiode-basics, 2022. Accessed: 2022-11-10.

[30] Mouser Electronics. First sensor ps100-6b thd. https://www.mouser.com/ProductDetail/First-Sensor/5000025, 2022. Accessed: 2022-11-10.

[31] Peter Adam Hoeher Jan Sticklus, Martin Hieronymi. Effects and constraints of optical filtering on ambient light suppression in led-based underwater communications. *Sensors*, 2018.

[32] Edmund Optics. Hard coated od 4.0 50nm bandpass filters. https://www.edmundoptics.com/f/hard-coated-od-4-50nm-bandpass-filters/14321/, 2022. Accessed: 2022-11-18.

[33] Winfield Hill Paul Horowitz. *Operational Amplifiers*, pages 223–233. Cambridge University Press, New York, NY, 2021.

[34] Texas Instruments. Ths4631. https://www.ti.com/product/THS4631, 2022. Accessed: 2022-11-10.

[35] Winfield Hill Paul Horowitz. *4x.3 Transresistance Amplifiers*, pages 283–298. Cambridge University Press, New York, NY, 2021.

[36] Robert A. Pease. *Bandpass Filters*, pages 225–245. Elseiver, Burlington, MA, 2008.

[37] New Mexico Institute of Mining and Technology. Ee 212l: Multiple feedback topology band-pass filter and the fourier series. http://www.ee.nmt.edu/~wedeward/EE212L/SP17/MultipleFeedbackTopologyBPF.html, 2017. Accessed: 2022-11-10.

[38] Texas Instruments. Filter designer. https://www.ti.com/design-resources/design-tools-simulation/filter-designer.html, 2022. Accessed: 2022-11-10.

[39] New Mexico Institute of Mining and Technology. Ltc1440 ultralow power single/dual comparator with reference. analog.com/en/products/ltc1440.html#product-overview, 2022. Accessed: 2022-11-10.

[40] Winfield Hill Paul Horowitz. *12.3 Comparators*, pages 809–816. Cambridge University Press, New York, NY, 2021.

[41] Mouser Electronics. Ad5220bnz10. https://www.mouser.com/ProductDetail/Analog-Devices/AD5220BNZ10, 2022. Accessed: 2022-11-10.

[42] James Bryant. Using op amps as comparators. https://www.analog.com/media/en/technical-documentation/application-notes/AN-849.pdf, 2011. Accessed: 2022-11-17.

[43] Blue Robotics. Blue robotics 2, 3 and 4-inch series. https://bluerobotics.com/product-category/watertight-enclosures/locking-series/, 2022. Accessed: 2022-11-19.

[44] Alan B. Coppens James V. Sanders Lawrence E. Kinsler, Austin R. Frey. *Transmission from one fluid to another: oblique incidence*, pages 155–160. Hamilton Press, Danvers, MA, 1976.

[45] Chris Woodley. Utilizing advanced materials to improve efficiency of uv-leds. https://sc.edu/study/colleges_schools/engineering_and_computing/news_events/news/2021/utilizing_advanced_materials_to_improve_efficiency_of_uv_leds.php, 2021. Accessed: 2022-11-21.

[46] Haiding Sun. A massive boost for uv led efficiency. https://compoundsemiconductor.net/article/110953/A_Massive_Boost_For_UV_LED_Efficiency/feature, 2020. Accessed: 2022-10-25.

[47] Federal Highway Administration. Fundamentals of telecommunications. https://ops.fhwa.dot.gov/publications/telecomm_handbook/chapter2_03.htm, 2022. Accessed: 2022-11-27.

[48] Ilya A. Udovydchenkov and Ballard J. Blair. Estimation of clock drift in underwater acoustic instruments using propagation channel analysis. https://asa.scitation.org/doi/10.1121/1.4989131, 2017. Accessed: 2022-11-28.

[49] James W. O'Dell. Method 180.1: Determination of turbidity by nephelometry. *U.S. Environmental Protection Agency*, 1993.

[50] Winfield Hill Paul Horowitz. *The Art of Electronics*. Cambridge University Press, New York, NY, 2021.

APPENDIX A

A1: Receiver Bit Recognition Pseudocode

```
1  void setup()
2  {
3    /*set_up interrupts for the receiver I/O pin:
4     * If I/O pin goes from LOW to HIGH, interrupt is triggered and
5     * HIGH_INTERRUPT() function is executed
6     * If I/O pin goes from HIGH to LOW, LOW_INTERRUPT() function is executed
7     */
8
9    attachInterrupt(digitalPinToInterrupt(receiver_pin), HIGH_INTERRUPT, RISING);
10   attachInterrupt(digitalPinToInterrupt(receiver_pin), LOW_INTERRUPT, FALLING);
11
12   /*
13    * Declare the following values:
14    *
15    * bit_length - length of a single bit. For example, at 5kbps, 1 bit lasts 200us
16    *
17    * delta - a period of time to identify transition between 1 and 0. This value
18    * should be smaller than bit_length but larger than carrier wave pulse length
19    *
20    * timeout_amount - a length of time which would trigger an end/loss of message.
21    * Should be a length of about 10-20 bits depending on packet structure
22    *
23    * start_packet[] - a sequence of bits that enables the system to distinguish an
24    * actual message from noise. If a start packet is identified within interpreted
```

```
25      * message, it will be further processed (or disregarded otherwise).
26      */
27  }
28
29  void main_loop()
30  {
31    if (zero_timer > delta && one_timer > delta)
32    {
33      /* transition between one and zero is identified, calculate number
34       * of ones transmitted:
35       */
36      number_of_ones = (one_timer - delta) / bit_length;
37      add_ones(number_of_ones);
38
39      //stop one_timer and reset it to zero
40      reset_one_timer();
41    }
42    if (timeout_timer > timeout_amount)
43    {
44      //message ended, reset all flags and values.
45    }
46  }
47
48  void HIGH_INTERRUPT()
49  {
50    if (receiving_message == 0)
51    {
52      //a first bit of the message is being read, thus a receiving flag is set to 1:
53      receiving_message == 1;
54      start_one_timer();
55      start_timeout_timer();
56    }
57    if (zero_timer > delta && receiving_message == 1)
```

```
58    {
59      //transition between zero and one is identified:
60      start_one_timer();
61      number_of_zeros = zero_timer / bit_length;
62      add_zeros(number_of_zeros);
63    }
64    reset_zero_timer();
65    restart_timeout_timer();
66  }
67
68  void LOW_INTERRUPT()
69  {
70    start_zero_timer();
71  }
72
73  void add_ones(int number_of_ones)
74  {
75    /*Add a number of ones calculated into the message array:
76      For example, if current array is 010 and two ones are detected,
77      New message array becomes 11010*/
78    if (current_message[] == start_packet[])
79    {
80      //message recognized as valid (not noise) and will be further processed
81    }
82  }
83  void add_zeros(int number_of_zeros)
84  {
85    //same function as add_ones() above, but adds zeros to the message array
86    if (current_message[] == start_packet[])
87    {
88      //message recognized as valid (not noise) and will be further processed
89    }
90  }
```